Deformation and stability of a viscous electrolyte drop in a uniform electric field

Qiming Wang, Manman Ma, and Michael Siegel

Phys. Rev. Fluids **4**, 053702 — Published 8 May 2019

DOI: 10.1103/PhysRevFluids.4.053702

Deformation and stability of a viscous electrolyte drop in a uniform electric field

Qiming Wang,[1] Manman Ma,[2,*] and Michael Siegel[1]

[1] *Department of Mathematical Sciences and Center for Applied Mathematics and Statistics, New Jersey Institute of Technology, Newark, NJ 07102, USA*

[2] *School of Mathematical Sciences, Tongji University, Shanghai 200092, China*

Abstract

We study the deformation and breakup of an axisymmetric electrolyte drop which is freely suspended in an infinite dielectric medium and subjected to an imposed electric field. The electric potential in the drop phase is assumed small, so that its governing equation is approximated by a linearized Poisson-Boltzmann or modified Helmholtz equation (the Debye-Hückel regime). An accurate and efficient boundary integral method is developed to solve the low-Reynolds-number flow problem for the time-dependent drop deformation, in the case of arbitrary Debye layer thickness. Extensive numerical results are presented for the case when the viscosity of the drop and surrounding medium are comparable. Qualitative similarities are found between the evolution of a drop with a thick Debye layer (characterized by the parameter $\chi \ll 1$, which is an inverse dimensionless Debye layer thickness) and a perfect dielectric drop in an insulating medium. In this limit, a highly elongated steady state is obtained for sufficiently large imposed electric field, and the field inside the drop is found to be well approximated using slender body theory. In the opposite limit $\chi \gg 1$, when the Debye layer is thin, the drop behaves as a highly conducting drop, even for moderate permittivity ratio $Q = \epsilon_1/\epsilon_2$, where ϵ_1, ϵ_2 is the dielectric permittivity of drop interior and exterior, respectively. For parameter values at which steady solutions no longer exist, we find three distinct types of unsteady solution or breakup modes. These are termed conical end formation, end splashing, and open end stretching. The second breakup mode, end splashing, resembles the breakup solution presented in a recent paper [R. B. Karyappa *et al.*, J. Fluid Mech. **754**, 550-589 (2014)]. We compute a phase diagram which illustrates the regions in parameter space in which the different breakup modes occur.

* Corresponding author: mamm@tongji.edu.cn

I. INTRODUCTION

The behavior of a viscous liquid drop immersed in a viscous surrounding fluid and acted on by an imposed electric field is a classical problem which has been extensively studied for over one hundred years. It is known that a mismatch in electrical properties between the fluids results in a jump in electric stress at the drop interface. In the case of a drop subjected to a uniform far-field electric field, non-uniform tractions at the drop surface lead to deformation of the interface and, for a sufficiently large imposed field, breakup of the drop. This problem arises in a number of important applications, including electrosprays, electrohydrodynamic atomization, breakup of droplets in thunderstorms, microfluidic processes, and others. A thorough review of the topic can be found in [1–5].

For either the case of a perfect dielectric or a perfectly conducting drop in an insulating medium the electric field modifies the normal stress at the interface but does not affect the tangential stress. The normal interfacial electric stress is balanced by surface tension, but the lack of a tangential electric stress to balance viscous stresses means that there can be no fluid flow when the drop reaches a steady-state shape. This leads to prolate steady-state drop shapes, as shown in a number of early studies [6–11]. A theoretical prediction of the steady-state solution branch based on a spheroidal approximation of the equilibrium drop shape is given in [10, 12]. Above a critical permittivity ratio $Q^c \simeq 20.8$, the theoretical steady solution branch forms an 'S' shape and is no longer single valued. Time-dependent boundary integral computations [13] of dielectric or non-conducting drops for Q greater than this critical value, starting from a spherical shape, converge to steady state profiles on the solution branch for sufficiently small electric field strength as measured by the electric capillary number $E_b = \epsilon_2 \mathscr{E}^2 R/\gamma$, where $\mathscr{E}$ is the applied field strength, R is the undeformed drop radius, and γ is the surface tension. However, beyond a critical electric field strength E_b^c associated with the first turning point on the solution branch, the evolving drop forms a pointed tip and the numerics break down before reaching the steady-state shape. This gives, in effect, a critical permittivity ratio Q^c and electric field strength E_b^c above which steady drop shapes are no longer observed. We note that steady-state shapes on the upper branch could be obtained in the numerics if the initial drop shape was sufficiently close to equilibrium [13], or by using other models [14]. When Q is less than the critical value, the boundary integral computations converge to the steady state for any electric field strength.

The pointed drop shape that occurs above a critical permittivity ratio Q and electric field strength was first investigated by G. I. Taylor for conducting water droplets in [10] and is known as a Taylor cone. Later theoretical work includes predictions of the conical-end angles of a Taylor cone [15–18]. It is worth noting that Taylor's analysis [10] is in fact based on a local solution that assumes a steady or equilibrium cone shape while in experiments the dynamics is often observed to be unsteady, with a thin, charged fluid jet emitted from the end of the conical or pointed tip in a process known as tipstreaming [19]. A recent review on the topic of Taylor cones in two-phase flow can be found in [20].

In addition to the prolate drop profiles mentioned above, experiments [9] in weakly conducting fluids show the presence of oblate drop shapes and non-zero fluid velocity even after a drop has reached a steady-state shape. These characteristics are not captured by the perfect dielectric and perfect conductor models. To explain these features, Taylor proposed the so-called leaky dielectric [21] or Taylor-Melcher (TM) model [2] for weakly conducting fluids, which has been widely and successfully applied to many problems in electrohydrodynamics (see, e.g., [22–28] in addition to the references below). The leaky dielectric model allows charge to accumulate at a fluid-fluid interface, and tangential electric stresses generated by this surface charge along with charge convection are found to be important for predicting oblate steady-state drop shapes, steady fluid motion, and unsteady breakup in isolated drops acted on by an electric field [29, 30]. The model has been used extensively in numerical studies of the steady deformation and unsteady breakup of an isolated drop in an imposed electric field, see e.g., [13, 29–33]. The results of these studies are in qualitative agreement with experiments involving weak electrolytes, although quantitative agreement is sometimes lacking. In particular, the numerical simulations capture the two main drop breakup modes observed in experiments [9, 11, 34, 35]. These are (i) end pinching, in which the drop elongates and forms fluid blobs at its ends that eventually pinch off, and (ii) tipstreaming, i.e., the formation of a Taylor cone, followed by emission of a thin charged fluid jet or a series of small droplets from the pointed tip. Tipstreaming from a viscous drop or fluid layer in an imposed electric field has been studied by finite element numerical simulations of the leaky dielectric model [19, 29]. In particular, these studies demonstrate the importance of charge convection and tangential electric stress at the interface in the phenomena of fluid ejection from Taylor cones. However, various experiments also report discrepancies between the TM model and experimental results (see for example Vizika and Saville [36] and Ha and Yang

[34]), which suggest the necessity of further modeling work. A thorough review on the TM model can be found in Melcher and Taylor [2], Saville [37], and Vlahovska [38].

In recent years there has been renewed interest in more detailed electrokinetic models for systems of drops and bubbles which incorporate equations governing the dynamics of bulk ionic charge. Theoretical studies have often focussed on the asymptotic analysis in the thin Debye layer limit of the electrokinetic equations for various physical problems [39–42]. There has been much less work on the direct numerical simulation of the full electrokinetic equations. Berry et al. [43] developed a combined level-set/volume-of-fluid method to simulate the Poisson-Nernst-Planck electrokinetic model for liquid-liquid interfaces. Pillai [14, 44] employed the method of [43] to study the deformation and breakup of an isolated electrolyte drop suspended in an insulating phase and acted on by an imposed electric field. Their results include computations of tip streaming drops. Related numerical work includes [45–47]. A strong motivation for theoretical and numerical analysis of the electrokinetic models is their significance in microfluidic devices, for which electrokinetic techniques have been among the most important methods for the manipulation of drops and bubbles [48].

In this paper, we modify the traditional model for a perfect dielectric drop in an insulating medium by assuming that the fluid inside the drop is an electrolyte, while keeping the exterior fluid as nonionic. We avoid the difficulty of solving the full nonlinear problem for the ion dynamics, as in [14, 44], by employing the Debye-Hückel approximation for the electric potential inside the drop, which results in a linearized Poisson-Boltzmann or modified Helmholtz equation. Our model is therefore less general than the full electrokinetic model of [14, 44], but has the advantage that the governing equations allow a Green's function formulation, which enables the development and application of a highly accurate boundary integral numerical method. This surface based numerical method can effectively compute for much thinner Debye layers (i.e., for $\chi \gg 1$) than is possible for the full electrokinetic model. A similar model was previously presented in Hua et al. [49], but there the focus is on analytical theory for small drop deformation. We go beyond this and carry out a more comprehensive numerical investigation.

Numerical computations based on a boundary integral formulation for the problem of freely suspended drops in an electric field have been popular due to their high accuracy and relative simplicity [13, 16, 30, 33, 50–54]. When the electric potential is governed by Laplace's equation, there is an analytical expression for the axisymmetric version of the

Green's function, i.e., the azimuthal part of the surface integral can be done analytically. This reduces the dimension of the boundary integrals and leads to a significant reduction in computational cost. However, this is not the case for the modified Helmholtz equation that arises here from linearizing the Poisson-Boltzmann equation. Although accurate numerical schemes to solve boundary integral formulations of Laplace and Helmholtz equations in axisymmetric geometries have been developed (see [55] and references therein), one of the main contributions in this paper is to develop a scheme to accurately and efficiently compute the Green's function for the modified Helmholtz equation and apply it to a moving boundary problem. In this way, we extend previous studies to assess the effect of ions on drop deformation in the case of arbitrary Debye-layer thickness. For numerical efficiency, our results are specialized to the case when the viscosity of the drop and surrounding medium are comparable.

Along with the numerical simulations, we also carry out a slender-body analysis (in the case of highly elongated drops) starting from the boundary-integral equations to approximate the electric field inside the drop. A correction term to the results of [15] that takes into account the presence of ions is derived, and the result is shown to agree reasonably well with simulations of the full problem.

The analysis and numerics are used to find steady state solution branches and unsteady breakup modes over a wide range of parameter values. These solutions are found to be in good agreement with previous computations [13, 17, 51] in the limiting cases of a perfect conductor or perfect dielectric, but exhibit some differences when compared to simulations based on the full electrokinetic model in [14]. For parameter values at which steady solutions no longer exist, we find three distinct types of unsteady solution or breakup modes, which are termed conical end formation, end splashing, and open end stretching (see Section IV B for examples of these breakup modes). Similar breakup phenomena have been previously reported in simulations of perfect conductor, perfect dielectric, and leaky dielectric models [13, 17, 30, 53]. However, there are some important differences in the results here.

To maintain simplicity, we do not allow for charge to accumulate at the interface. Thus, like the perfect dielectric and perfect conductor models, there is no tangential electric stress at the interface (see Section II for a detailed discussion). The general expectation is that drop breakup by tipstreaming or pinch-off does not occur in the absence of such tangential interface stresses [29]. Although our model does not capture the tip streaming of thin charged

jets from a Taylor cone, as in [14, 29], a main result of this paper is the computation of breakup modes without tangential interface stress, as shown in Section IV B. One of these breakup modes, end splashing, involves the formation of a Taylor-cone-like structure, followed by the emission or discharge of a thin axisymetric sheet of fluid which subsequently can pinch off. This breakup mode is not seen in computations of the leaky dielectric model, but is very similar to that observed in experiments and simulations of an electrokinetic model in [56], based on a pendant drop geometry. A similar breakup mode is observed in experiments on high conductivity drops and simulations of a perfect conductor model at small viscosity ratio ($Q \to \infty$ and $\lambda \lesssim 0.05$) in [53]. Here, however, we find that end-splashing also occurs at a finite conductivity ratio Q and for unit viscosity ratio $\lambda = 1$, suggesting that electrokinetic effects can promote this type of breakup. Preliminary computations using our model at a small viscosity ratio, to be reported elsewhere, also exhibit the end-splashing breakup mode.

The model presented here is formally valid for small potential, or more precisely, when $e\phi/(k_B T) \ll 1$. However, we will sometimes also apply it to cases with large deformation and potentials (e.g., Figure 10) which may be beyond its range of formal validity. Nevertheless, qualitative similarities between solutions to our model and behavior observed in the experiments of [53, 56], even at relatively large potentials, are encouraging. A discussion of the Debye-Hückel theory and its limitations is given in [57].

The paper is organized as follows. We begin in Section II with a complete description of the equations governing the electric field, viscous flow and the boundary conditions. In Section III, the problem is reformulated as a system of boundary integral equations and the numerical method is introduced. Numerical results are presented in Section IV. We summarize the effect of ions on the drop's steady deformation and unsteady breakup behavior. Closing remarks are provided in Sec. V. In Appendix A, we present the formulations of the Green's function and its derivatives for the modified Helmholtz equation, as well as results demonstrating the accuracy of our numerical scheme in computing the Green's functions. In Appendix B, we present a brief derivation of the small deformation theory for our problem. This is used to compare with and partially validate our numerical results. Finally, details of the slender-body analysis are presented in Appendix C.

II. MATHEMATICAL FORMULATION

A. Electrokinetic equations

We consider the dynamics of an electrolyte fluid drop with viscosity $\lambda\mu$ (region 1) immersed in a dielectric (nonionic) medium with viscosity μ (region 2), as shown in Figure 1. Cylindrical polar coordinates $\boldsymbol{x} = r\boldsymbol{e}_r + z\boldsymbol{e}_z$ are used with the z-axis alligned with the drop's axis of symmetry. The surrounding medium is considered as a perfect dielectric and the electric potential ϕ_2 satisfies Laplace equation with a far field condition $\phi_2 \to -\mathscr{E}z$ due to the applied electric field $\mathbf{E} = \mathscr{E}\boldsymbol{e}_z$.

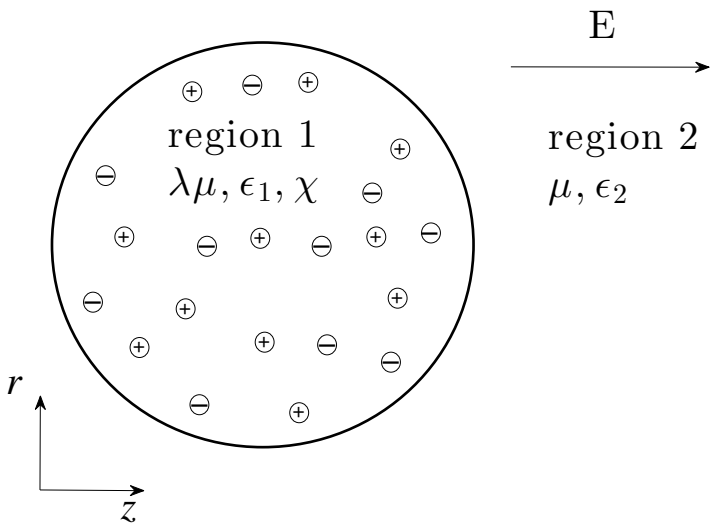

FIG. 1. An electrolyte fluid drop with viscosity $\lambda\mu$ is surrounded by a nonionic fluid with viscosity μ. A constant electric field, directed along the z-axis, is imposed in the far field.

In the drop phase, the electric potential is governed by Poisson's equation,

$$-\epsilon_1\nabla^2\phi_1 = \rho = \sum_{i=1}^{N} ez_ic_i, \tag{1}$$

with ϵ_1 the dielectric constant, ρ the bulk volume charge density, z_i the valence of species i and e the elementary charge. We assume that the ions are in thermo-equilibrium and that their concentration follows a Boltzmann-distribution [58–60],

$$c_i = c_i^0 e^{-z_i e(\phi_1-\phi_0)/(k_BT)}, \tag{2}$$

where ϕ_0 is a reference potential, which is set to zero without loss of generality, k_B is the Boltzmann constant, and T is the absolute temperature. We consider a symmetrical electrolyte with $z_1 = -z_2 = z$ and $c_1^0 = c_2^0 = c^0$, which leads to an odd symmetry of the potential ϕ_1 with respect to the plane $z = 0$, where $\phi_1 \equiv 0$. We take c_i^0 to be the constant bulk concentration of ion species i far from the interface when this bulk state exists (e.g., for a thin Debye layer), and otherwise take it to be the ion concentration on the plane $z = 0$. The neutral bulk condition $\sum_{i=1}^{2} z_i c_i^0 = 0$ is assumed to hold. We introduce

$$\beta = \frac{\mathscr{E} eR}{k_B T} \tag{3}$$

which measures the ratio of the imposed field potential over the thermal potential. Using R, $\mathscr{E}R$ and c^* as the characteristic length, electric potential and ion concentration in equation (1), where R is the unperturbed drop radius, $\mathscr{E}$ is the uniform electric field at infinity, and $c^* = \int_\Omega c_i \, dV / \int_\Omega dV$ is the average concentration of ion species i in drop region Ω (which is the same for $i = 1, 2$), we obtain the Poisson-Boltzmann equation in dimensionless form

$$-\nabla^2 \phi_1 = \frac{eRc^*}{\epsilon_1 \mathscr{E}} \sum_{i=1}^{2} z_i c_i^0 e^{-\beta z_i \phi_1}. \tag{4}$$

In the case of small applied (drop phase) potential $|\beta\phi_1| \ll 1$, the ion concentration is approximated as $c_i \approx c_i^0(1 - \beta z_i \phi_1)$ and ionic mass conservation in the drop combined with symmetry of the potential ϕ_1 gives $c_i^0 = 1$. Thus, Eq. (4) simplifies at leading order to the linearized Poisson-Boltzmann or modified Helmholtz equation,

$$\nabla^2 \phi_1 = \chi^2 \phi_1, \tag{5}$$

where

$$\chi^2 = \frac{2z^2 e^2 R^2 c^*}{\epsilon_1 k_B T}. \tag{6}$$

This linearized equation, also known as Debye-Hückel approximation, is widely used in various problems involving electrolyte solutions [49, 58–63]. An advantage of (5) is that there is a Green's function representation of the solution, which is evaluated using a highly accurate boundary integral numerical method. Since drop breakup can require large applied voltage, we will sometimes apply the approximation (5) in situations in which it is not formally valid.

At the drop interface, we have the boundary conditions

$$\phi_1 = \phi_2, \quad Q\phi_{1n} = \phi_{2n}, \tag{7}$$

where $Q = \epsilon_1/\epsilon_2$. This specifies that no ionic charge accumulates at the interface, a condition used in the electrolyte-drop model of [49].

B. Fluid motion and stress boundary conditions

The fluid motion is approximated by Stokes equations, which are nondimensionalized using the spherical drop radius R for lengths, γ/R for pressure, $\mathscr{E}R$ for potential, and γ/μ for velocities, with γ the surface tension. After replacing $\nabla^2\phi_1$ by $\chi^2\phi_1$ from (5), we have

$$-\nabla p_1 + \alpha\phi_1\nabla\phi_1 + \lambda\nabla^2\boldsymbol{u}_1 = 0, \quad \nabla\cdot\boldsymbol{u}_1 = 0, \tag{8}$$

$$-\nabla p_2 + \nabla^2\boldsymbol{u}_2 = 0, \quad \nabla\cdot\boldsymbol{u}_2 = 0. \tag{9}$$

In the above,

$$\alpha = \chi^2 E_b Q \ \text{ with } \ E_b = \epsilon_2\mathscr{E}^2 R/\gamma, \tag{10}$$

where the latter quantity is an electric capillary number which measures the ratio of Maxwell or electric stress to capillary pressure. The stress balance on the interface is written as

$$[\boldsymbol{\mathcal{T}}\cdot\boldsymbol{n}]_2^1 = [\boldsymbol{\sigma}\cdot\boldsymbol{n}]_2^1 - \triangle\boldsymbol{f}^e = -\kappa\boldsymbol{n}, \tag{11}$$

where $\boldsymbol{\sigma} = -p\boldsymbol{I} + 2\lambda_i\boldsymbol{e}$ is the hydrodynamic stress tensor with $\lambda_1 = \lambda$ and $\lambda_2 = 1$, $\boldsymbol{e}$ is the symmetric part of the velocity gradient, $\boldsymbol{n}$ is the outward unit normal, and κ is the interface curvature, taken as positive for a convex surface. Here $[\cdot]_2^1$ denotes the jump across the interface, with the convention that it is the limit as the interface is approached from the interior domain (region 1) minus the limit from the exterior domain (region 2). The Maxwell stress, or electric contribution to the stress balance, is directed normally to the interface and is given by

$$\triangle\boldsymbol{f}^e = \frac{E_b(Q-1)}{2}\left(QE_{1n}^2 + E_t^2\right)\boldsymbol{n}, \tag{12}$$

where E_{1n} and E_t are normal and tangential components of electric field $\boldsymbol{E} = -\nabla\phi$ in region 1 respectively (see Sherwood [13], Lac and Homsy [33], Miksis [50]). The jump in tangential stress at the interface is $\epsilon_2 E_t(E_{2n} - QE_{1n})$ [13] and is zero in view of the boundary condition (7) for a charge free surface. Far from the drop, $\phi_2 \to -z$ as $|\boldsymbol{x}| \to \infty$.

III. BOUNDARY INTEGRAL METHOD

A. Integral equations

We reformulate the electrostatic problem as a system of boundary integral equations using classical potential theory [64]. Denote the Green's function for the modified Helmholtz equation by G^{χ}_{3D}; expressions for this Green's function are presented in Appendix A. The electric potentials ϕ_1 and ϕ_2 in regions 1 and 2 satisfy

$$\frac{1}{2}\phi_1(\boldsymbol{x_0}) + \int_S \phi_1(\boldsymbol{x})\frac{\partial G^{\chi}_{3D}}{\partial n_x}(\boldsymbol{x},\boldsymbol{x_0})\ dS(\boldsymbol{x}) = \int_S \frac{\partial \phi_1}{\partial n}(\boldsymbol{x}) G^{\chi}_{3D}(\boldsymbol{x},\boldsymbol{x_0})\ dS(\boldsymbol{x}), \tag{13}$$

$$-\frac{1}{2}\left(\phi_2(\boldsymbol{x}_0) - \phi_\infty(\boldsymbol{x_0})\right) + \int_S \left(\phi_2(\boldsymbol{x}) - \phi_\infty(\boldsymbol{x})\right)\frac{\partial G^{0}_{3D}}{\partial n_x}(\boldsymbol{x},\boldsymbol{x_0})\ dS(\boldsymbol{x}),$$

$$= \int_S \frac{\partial\left(\phi_2 - \phi_\infty\right)}{\partial n}(\boldsymbol{x}) G^{0}_{3D}(\boldsymbol{x},\boldsymbol{x_0})\ dS(\boldsymbol{x}), \tag{14}$$

where $\phi_\infty = -z$ is the imposed far-field electric potential. We note that setting $\chi = 0$ in (13) recovers the case of a perfect dielectric drop, in which electrolyte is not present in the interior (see [50]).

The standard boundary integral formulation of the Stokes flow problem for the fluid velocity is modified to include the electrostatic forcing. Starting from the Lorentz reciprocal relation [65], we obtain

$$\boldsymbol{u}_1(\boldsymbol{x}_0) = \frac{\alpha}{8\pi\lambda}\int_V \phi_1(\boldsymbol{x})\nabla\phi_1(\boldsymbol{x})\cdot\boldsymbol{J}(\boldsymbol{x},\boldsymbol{x_0})\ dV(\boldsymbol{x}) + \frac{1}{8\pi\lambda}\int_S \boldsymbol{n}(\boldsymbol{x})\cdot\boldsymbol{\sigma}_1(\boldsymbol{x})\cdot\boldsymbol{J}(\boldsymbol{x},\boldsymbol{x_0})\ dS(\boldsymbol{x})$$

$$+\frac{1}{8\pi}\int_S \boldsymbol{n}(\boldsymbol{x})\cdot\boldsymbol{K}(\boldsymbol{x},\boldsymbol{x_0})\cdot\boldsymbol{u}(\boldsymbol{x})\ dS(\boldsymbol{x}), \tag{15}$$

$$\boldsymbol{u}_2(\boldsymbol{x}_0) = -\frac{1}{8\pi}\left(\int_S \boldsymbol{n}(\boldsymbol{x})\cdot\boldsymbol{\sigma}_2(\boldsymbol{x})\cdot\boldsymbol{J}(\boldsymbol{x},\boldsymbol{x_0})\ dS(\boldsymbol{x}) + \int_S \boldsymbol{n}(\boldsymbol{x})\cdot\boldsymbol{K}(\boldsymbol{x},\boldsymbol{x_0})\cdot\boldsymbol{u}(\boldsymbol{x})\ dS(\boldsymbol{x})\right), \tag{16}$$

where $\boldsymbol{J}$ and $\boldsymbol{K}$ are the Stokeslet and Stresslet Green's functions for Stokes flow, and $\boldsymbol{x}_0$ is located in regions 1 and 2 in (15) and (16), respectively. The first term on the right hand side of (15) is transformed into a surface integral by using the divergence free property of the Stokeslet, namely,

$$\nabla\cdot\boldsymbol{J} = 0, \tag{17}$$

which leads to

$$\int_V \phi_1(\boldsymbol{x})\nabla\phi_1(\boldsymbol{x})\boldsymbol{J}(\boldsymbol{x},\boldsymbol{x_0})\ dV(\boldsymbol{x}) = \frac{1}{2}\int_V \nabla_{\boldsymbol{x}}\cdot\left(\phi_1^2(\boldsymbol{x})\boldsymbol{J}(\boldsymbol{x},\boldsymbol{x_0})\right)\ dV(\boldsymbol{x}), \tag{18}$$

$$= \frac{1}{2}\int_S \phi_1^2(\boldsymbol{x})\boldsymbol{J}(\boldsymbol{x},\boldsymbol{x_0})\cdot\boldsymbol{n}(\boldsymbol{x})\ dS(\boldsymbol{x}), \tag{19}$$

where (19) follows (18) by the divergence theorem. As $\boldsymbol{x}_0$ approaches interface, the integral equations can be combined to one equation by using (11),

$$\boldsymbol{u}(\boldsymbol{x}_0) = -\frac{1}{4\pi(1+\lambda)}\int_S \boldsymbol{J}(\boldsymbol{x},\boldsymbol{x_0})\cdot\triangle\boldsymbol{F}^e(\boldsymbol{x})\ dS(\boldsymbol{x}) \\ - \frac{1-\lambda}{4\pi(1+\lambda)}\int_S \boldsymbol{n}(\boldsymbol{x})\cdot\boldsymbol{T}(\boldsymbol{x},\boldsymbol{x_0})\cdot\boldsymbol{u}(\boldsymbol{x})\ dS(\boldsymbol{x}), \tag{20}$$

where ϕ_s is the electric potential on the interface S and

$$\triangle\boldsymbol{F}^e = \left(\kappa - \frac{\alpha}{2}\phi_s^2\right)\boldsymbol{n} - \triangle\boldsymbol{f}^e, \tag{21}$$

where α is given in (10) and $\triangle\boldsymbol{f}^e$ is given by (12). Similar integral equation formulations for a viscous drop in an electric field have appeared in [13, 33, 50], and [65, 66] provides more details in the derivation, as well as numerical implementations. Note that the additional term $\alpha\phi_s^2$ in (21) is a consequence of the electric body force in the Stokes equation. This term can also be understood via a modified or effective pressure $\hat{p}_1 = p_1 - \frac{\alpha}{2}\phi_1^2$ in (8), which similarly implies (21). In the limit of a perfect conductor ($\chi \to \infty$), $\phi_1 = 0$, whereas in the limit of a perfect dielectric drop, $\chi \to 0$, hence $\alpha \to 0$. Therefore, this additional term vanishes in both extreme cases.

B. Computation of Green's functions

The axisymmetric version of the free space Green's function for Laplace's equation (defined as the azimuthal integral of the 3D Green's function) can be expressed in closed form, see for example, [66],

$$G^0(z,z_0,r,r_0) = \int_0^{2\pi} G^0_{3D}(z,z_0,r,r_0,\phi,\phi_0)d\varphi = \frac{K(k)}{\pi\sqrt{(z-z_0)^2+(r+r_0)^2}}, \tag{22}$$

where $G^0_{3D}(z,z_0,r,r_0,\phi,\phi_0) = ((z-z_0)^2+r^2+r_0^2-2rr_0\cos(\phi-\phi_0))^{-1/2}/(4\pi)$ is the Green's function for the 3D Laplace's equation in cylindrical coordinates, $k^2 = 4rr_0/\left[(z-z_0)^2+(r+r_0)^2\right]$

and $k \leq 1$. Here $K(k)$ is the complete elliptical integral function of first kind,

$$K(k) = \int_0^{\pi/2} \frac{d\theta}{\sqrt{1 - k^2 \cos^2 \theta}}. \tag{23}$$

The axisymmetric Green's function for the modified Helmholtz equation, however, does not have an analytical expression. Starting from the Green's function for the modified Helmholtz equation in cylindrical coordinates, we write the axisymmetric version as follows:

$$\begin{aligned} G^{\chi}(z, z_0, r, r_0) &= \frac{1}{4\pi} \int_0^{2\pi} \frac{\exp\left(-\chi \left[(z - z_0)^2 + r^2 + r_0^2 - 2rr_0 \cos u\right]^{1/2}\right)}{\left((z - z_0)^2 + r^2 + r_0^2 - 2rr_0 \cos u\right)^{1/2}} du \\ &= \frac{1}{4\pi} \int_0^{2\pi} \frac{\exp\left(-\chi \left[(z - z_0)^2 + (r + r_0)^2 - 4rr_0 \cos^2(u/2)\right]^{1/2}\right)}{\left((z - z_0)^2 + (r + r_0)^2 - 4rr_0 \cos^2(u/2)\right)^{1/2}} du \\ &= \frac{k}{2\pi (rr_0)^{1/2}} \int_0^{\pi/2} \frac{\exp\left(-\Lambda \left[1 - k^2 \cos^2 \theta\right]^{1/2}\right)}{\left(1 - k^2 \cos^2 \theta\right)^{1/2}} d\theta, \end{aligned} \tag{24}$$

where $\Lambda = 2\chi (rr_0)^{1/2}/k$. When $|\Lambda| \ll 1$ or $|\Lambda| \gg 1$ in (24), the Green's function is expanded in an appropriate series for the numerical calculations in [67]. In the present study, we focus on the direct evaluation of (24) by proper quadrature.

Substitution of $t = \cos \theta$ into (24) results in

$$G^{\chi}(z, z_0, r, r_0) = \frac{k}{2\pi (rr_0)^{1/2}} \int_0^1 \frac{\exp\left(-\Lambda \left[1 - k^2 t^2\right]^{1/2}\right)}{\left(1 - k^2 t^2\right)^{1/2}} \frac{dt}{(1 - t^2)^{1/2}}. \tag{25}$$

Gauss-Chebyshev quadrature would seem a natural choice to integrate (25), treating $(1 - t^2)^{-1/2}$ as the weight function. However, our experience shows that Alpert quadrature [68] gives faster convergence and better performance. By recognizing $(1 - t)^{-1/2}$ as a singular function inside the integrand and setting $t = 1 - x$, (25) can be rewritten as

$$G^{\chi}(z, z_0, r, r_0) = \frac{k}{2\pi (rr_0)^{1/2}} \int_0^1 \frac{\exp\left(-\Lambda \left[1 - k^2 (1 - x)^2\right]^{1/2}\right)}{\left(1 - k^2 (1 - x)^2\right)^{1/2} (2 - x)^{1/2}} x^{-1/2} dx. \tag{26}$$

Alpert quadrature uses a hybrid Gauss-trapezoidal quadrature rule for the integration $\int_0^1 f(x) dx$ where $f(x) = g(x) x^{-1/2}$ and $g(x)$ is regular. The quadrature follows the formula (see [68] for more details)

$$T_n^{jkab}(f) = h \left(\sum_{i=1}^{j} u_i f(v_i h) + \sum_{i=0}^{m-1} f(ah + ih) + \sum_{i=1}^{k} w_i f(1 - x_i h) \right), \tag{27}$$

where the nodes $v_1, ..., v_j, x_1, ..., x_k$ and weights $u_1, ..., u_j, w_1, ..., w_k$ are given for known j, k, a, b which are related to the convergence order, here chosen as fourth order. The total number of nodes is denoted by $n = j + m + k$. This method is of high order accuracy when the Green's function is regular.

As $k \to 1$, i.e. Green's function (24) is close to singular and exhibits the same singular behavior as (22) for Laplace's equation. Simple calculation shows that the singular behavior of the normal gradient of G^χ is also the same as that of G^0. We add and subtract the singular Laplace kernel to obtain

$$G^\chi(z, z_0, r, r_0) = \frac{k}{2\pi(rr_0)^{1/2}} \int_0^1 \frac{\exp\left(-\Lambda\left[1-k^2t^2\right]^{1/2}\right) - 1}{\left(1-k^2t^2\right)^{1/2}} \frac{dt}{(1-t^2)^{1/2}} + G^0(z, z_0, r, r_0), \tag{28}$$

so that the first term is regular, and we use the hybrid quadrature method as described above. Meanwhile, the singularity in G^0 is treated in a standard way, via Gauss-log quadrature [26, 69]. Expressions for the gradient of the Green's function are given in Appendix A and the method of treating the singularity in derivatives of G^χ is the same as for G^χ. Furthermore, in Appendix A we provide sample calculations of both the Green's function and its derivatives, which demonstrates the accuracy and of our numerical method. We note that for thin Debye layers $\Lambda \gg 1$, and the main contribution to the integral in (28) is localized near $t = 1$ and $k = 1$. Resolution studies show that our computation of the Green's function has error of about 10^{-6} for Λ up to 1414, when $n = 2048$ is employed in the Alpert quadrature.

C. Numerical procedure

In this paper, we focus on the deformation of axisymmetric drops. The azimuthal part of the surface integrations in each of the integral equations is carried out analytically, except for the ones with Green's functions from the modified Helmholtz equations, for which Alpert quadrature is implemented as described above. The drop interface is discretized by $N + 1$ points, which divide it into N segments. The discretized equations assume the unknown 'densities' ϕ_s and $\boldsymbol{u}$ vary linearly between node points along the interface. On each boundary element, this gives an integral of the product of a linear (density) function and the Green's function. Integrations of this product are carried out in double precision using

six-point Gaussian quadrature when the element is regular. As $\boldsymbol{x}_0 \to \boldsymbol{x}$ the integrand is logarithmically singular, and Gauss-Log quadrature is used to handle the singularity (see also the implementation in [26]). The normal and curvature along the drop interface are calculated by fitting cubic splines, which is similar to Stone and Leal [70].

The linear system that results from discretizing an integral equation is solved by using the Fortran subroutine dgesv in LAPACK. After obtaining surface velocities, the drop interface is advanced by Euler's method via the kinematic condition. The full method is second order accurate in space and first order accurate in time. A solution is deemed to be in a steady state when $\max|u_n| < 10^{-4}$ along the drop interface. For the steady state calculations reported here, $N = 40 \sim 70$ is typically enough to resolve the interface. The code for the Stokes droplet without an electric field has been extensively tested and used in earlier work [71, 72]. When electrostatic fields are included in both the drop and surrounding phases in the simpler case of $\chi = 0$, the code has been validated against small deformation theory as well as the results in [13, 33], where good agreement is obtained. For example, in Figure 2 we compare the numerically computed electric potential ϕ_s for a spherical drop with an analytical prediction from Hua et al. [49], for a uniform imposed field with $\phi \to -z$ as

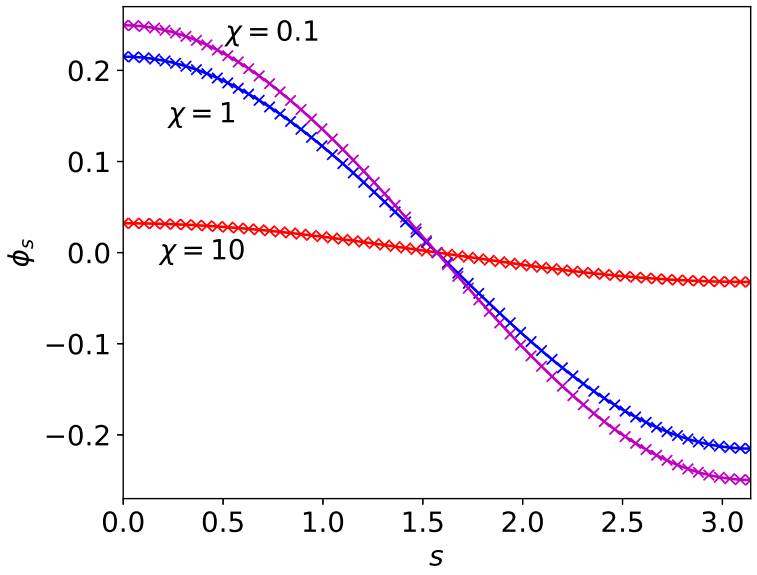

FIG. 2. Comparison of numerically computed results (solid lines) for the surface potential ϕ_s and analytical solutions (cross symbols) for a spherical particle, from [49]. Here $Q = 10$ and χ is indicated in the figure.

$\boldsymbol{x} \to \infty$. Parameter values are $Q = 10$ and $\chi = 0.1, 1, 10$. Excellent agreement is obtained.

If the drop deforms into a highly elongated spheroidal shape or a spindle shape with conical ends, an adaptive regridding scheme is employed. In particular, grid points are redistributed using cubic spline interpolation to be inversely proportional to local curvature, so that the density of points is high near conical ends. One check on the overall method is to compare our calculated results with those in Sherwood [13] (e.g. their Figure 3). The results are in excellent agreement (see also our Figure 5). If the drop becomes elongated and exhibits end pinching or other breakup modes, larger N is used (typically $N \sim 160$ to 320) together with adaptive time stepping. No special adaptive spatial regridding is applied in this case.

IV. RESULTS AND DISCUSSION

We focus the discussion on the case where the interior and exterior fluids have equal viscosity, i.e., $\lambda = 1$. The third term in equation (20) is then absent, which greatly simplifies the numerics, but also allows for a rich bifurcation diagram and wide variety of unsteady shapes. Results for $\lambda \neq 1$ will be reported elsewhere.

Parameters in experiments

Microfluidic drops as small as 1μm are routinely generated and manipulated in experiments, although studies on drop deformation and breakup commonly use millimeter-sized drops. Representative values of parameters in experiments are: $\mathscr{E} \simeq 10^5$ V/m, $D \simeq 10^{-9}$ m^2/s, $\mu \simeq 100 Pa{\cdot}s$ [37, 73] and $\gamma \simeq 10$ mN/m [53]. Assuming $R \simeq 1$mm and approximating $\epsilon_2 \simeq 80\epsilon_0$ (the permittivity of water), the electric capillary number at breakup is estimated as $E_b = \epsilon_2 \mathscr{E}^2 R/\gamma \simeq 10^{-1}$, consistent with the numerical results below. The conductivity σ in our electrokinetic model is related to the ion density by $\sigma = 2e^2 D c^0/(k_B T)$, assuming a symmetric 1:1 electrolyte. Using a representative bulk ion concentration $c^0 \simeq 10^{-7}$ moles/liter gives a conductivity $\sigma \simeq 10^{-9}$ S/m [37] with corresponding Debye layer thickness $\ell_D \simeq 10^{-6}$ m, so that $\chi \simeq 10^3$. A poorly conducting drop is obtained by specifying a thick Debye layer $\chi \lesssim 1$, although care is required to insure that the equilibrium assumption in (2) is satisfied. This necessitates that the charge relaxation time scale t_e be much shorter

than the time scale for fluid motion t_μ. Taking $t_e = R^2/(\chi^2 D)$ and $t_\mu = \mu/(\epsilon_2 \mathscr{E}^2)$ (which is a characteristic time for the Maxwell stress to deform the drop), we obtain $t_e/t_\mu = PeE_b/\chi^2$, where the Peclet number $Pe = \gamma R/(\mu D)$. Using the above parameters, we find $t_e/t_\mu << 1$ for a millimeter drop when $\chi >> 1$, but when $\chi \simeq 1$ it is necessary for $R \lesssim 10\mu$m to satisfy the condition on time scales. The latter estimate shows that the equilibrium assumption is consistent with a Debye layer thickness on the order of drop size only for a 10μm or smaller drop. Finally, the dimensionless potential is estimated as $\beta \simeq 10^3$. This suggests that $|\beta\phi_1|$ may not be small, except in the perfect conductor limit $\chi >> 1$ or $Q >> 1$ in which case $\phi_1 << 1$ (see e.g., Appendix B). However, as noted, we will apply the Debye-Hückel approximation, even when it may not be formally valid.

A. Steady state drops

In this section we show the computed steady states of drops in a uniform imposed electric field. We note that unless specified otherwise, the reported simulation time is rescaled following [74] as $t = \tilde{t}\gamma/2\pi R\mu(1+\lambda)$, where $\tilde{t}$ is dimensional time. Following other work we measure drop deformation using the Taylor deformation parameter

$$D_f = \frac{l-b}{l+b}, \tag{29}$$

where b and l are semi-axes of the drop at steady state perpendicular to and along the applied electric field, respectively. To compute the steady response curve we use continuation in the parameter E_b: once a steady state solution is obtained, we increase E_b to a larger value and use the steady solution at the previous E_b as initial data.

Figure 3 compares the drop deformation for fixed permittivity ratios $Q = 5$ and $Q = 50$ and a range of χ. The deformation curves follow small deformation theory (see (B6) in Appendix B) when E_b is relatively small. The deformation is seen to be greater when χ is larger, with the same imposed electric field E_b. This is because capillary pressure has a reduced effect, relative to electrostatic stresses, as χ is increased, per (21). This permits a more deformed surface before a local force balance between the capillary force and Maxwell (electrostatic) traction is reached. Increasing Q also tends to increase the deformation at a fixed imposed field strength.

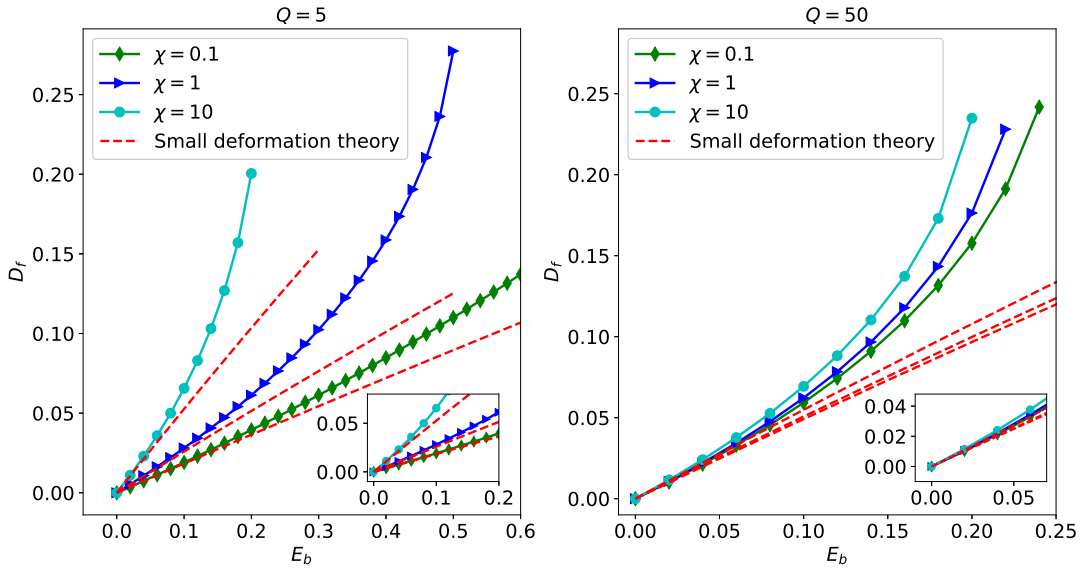

FIG. 3. Comparison between computed results (solid lines with filled symbols) and small deformation theory from [49] and Appendix B (dashed lines) with Q and χ indicated in the figure. Insets: Magnification of results near $E_b = 0$.

Conducting drops

In our model, there are two ways to approach the conducting drop limit: either $\chi \to \infty$ or $Q \to \infty$. The surface potential ϕ_s in either case tends to zero, as can be seen by taking the appropriate limit in the small deformation theory (see Appendix B). This theory also shows that the deformation for $\chi \gg 1$ and $Q \gg 1$ is given by $D_f \approx (9/16)E_b$, for $E_b \ll 1$. Figure 4 shows the steady deformation curves for various values of Q and χ which all correspond to a highly conducting liquid drop. As expected, the deformation curves nearly overlap each other. The critical value of E_b at which point steady solutions no longer exist is roughly the same for each branch and is about 0.21, which is consistent with the value reported for a perfectly conducting drop in Karyappa et al. [53] and Dubash and Mestel [51]. The maximum interface potential over all the steady solutions represented in the figure is less than 0.03.

Dielectric drops

When χ is small and Q is not too large (i.e., $\chi \lesssim 1$ and $Q \lesssim 10^1$) , the drop is close to a perfect dielectric suspended in an insulating medium (e.g., see the case $\chi = 0.1$ and $Q = 5$ in the left panel of Figure 3). We caution that time-dependent solutions to our model are unphysical in this perfect dielectric limit, as noted in Section IV, since the ratio of charge relaxation time scale to time scale for fluid motion, t_e/t_μ, is not small. Nevertheless, comparison of the simulations with the theoretical steady response curve provides a useful validation of the numerics. Steady solution branches for such nearly dielectric drops are shown in Figure 5, which extends the plot in Figure 3 to smaller values of χ and larger imposed field strength E_b. Instead of plotting the deformation as in Figure 3, we plot the aspect ratio l/b to which is better suited to the wide range of E_b used here. We also overlay both the analytical solution using the spheroidal approximation at $\chi = 0$ and the boundary integral solution for a perfect dielectric drop in an insulating medium (the analytical expression for the spheroidal approximation is available in Pillai et al. [14]). It is seen that the computed deformation curves for $\chi = 0$ and 0.01 almost exactly lie on top of the analytical

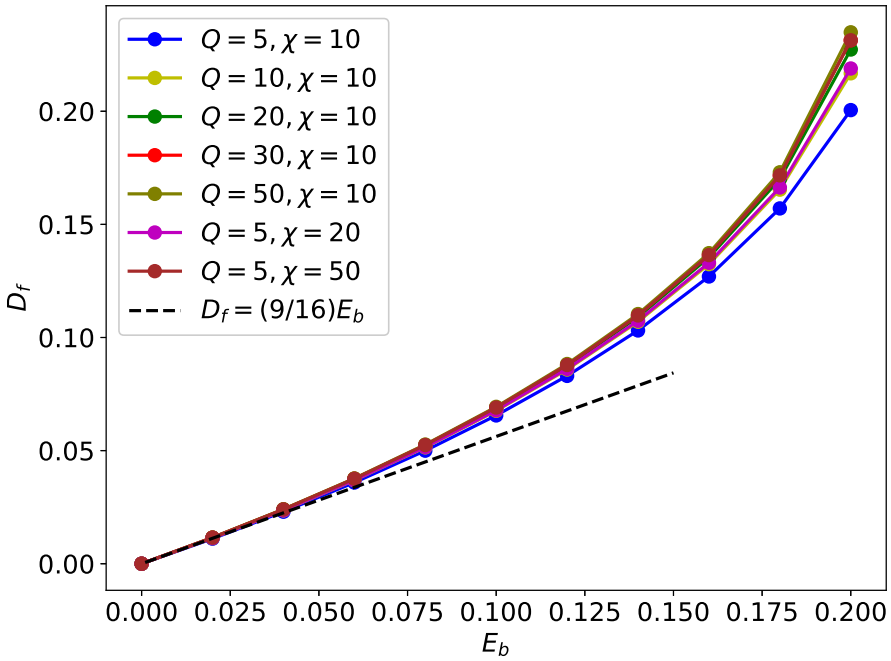

FIG. 4. Steady state deformation curves for various Q and χ, corresponding to a highly conducting drop, compared with the small deformation result $D_f = (9/16)E_b$.

curve. For $\chi = 0.1$, differences between the curves only occur when E_b is sufficiently large. Consistent with previous observations at small deformation, increasing χ promotes larger deformation for a given E_b. For $\chi = 0.2$ and 0.25, deviation from the insulating drop limit occurs at smaller E_b, as expected. An aspect ratio of $l/b \approx 4.4$ is quickly reached at about $E_b = 1.6$ for $\chi = 0.25$, beyond which the drop is found to be unstable and steady solutions no longer exist.

For larger Q (e.g., $Q = 50$ in Figure 6) the spheroidal approximation gives an 'S'-shaped curve [14, 37]. The steady solutions computed by our time-dependent simulations converge to the lower branch of the theoretical response curve as $\chi \to 0$. Using our model, it was not possible to capture the jump to the upper branch of the deformation curve. Instead, for E_b greater than the critical value $E_b \simeq 0.25$ at the turning point on the lower branch, an unsteady pointed drop develops and the numerics eventually break down, as discussed more fully in Section IV B. This is similar to the results of [13] using a dielectric model, but contrasts with the time-depedent simulations of [14] using a full electrokinetic model, which evolve to steady solutions on the upper branch. The latter discrepancy may be due

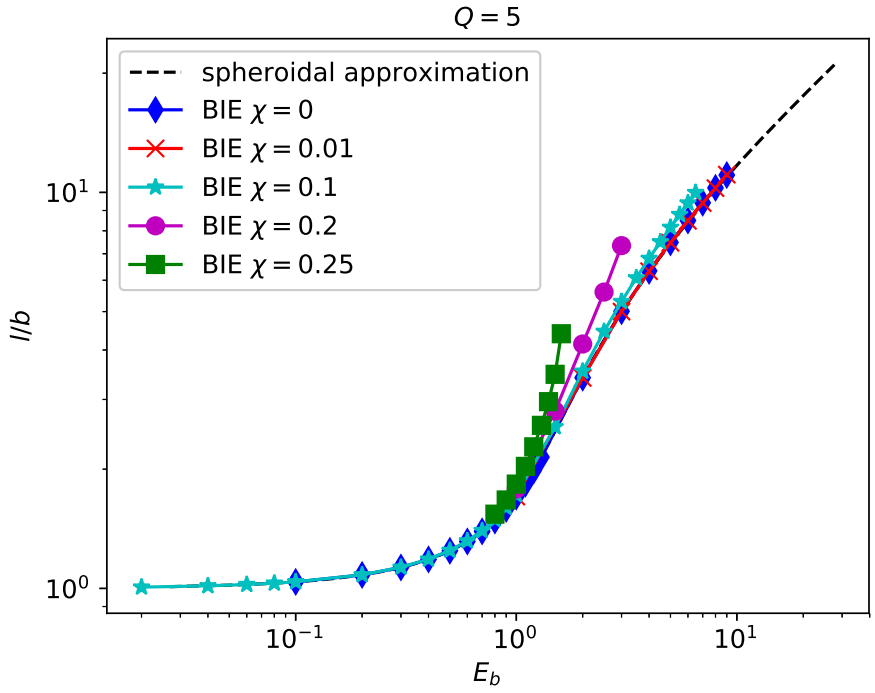

FIG. 5. Comparison of drop deformation for various χ and $Q = 5$ together with the analytical results based on a spheroidal approximation for $\chi = 0$.

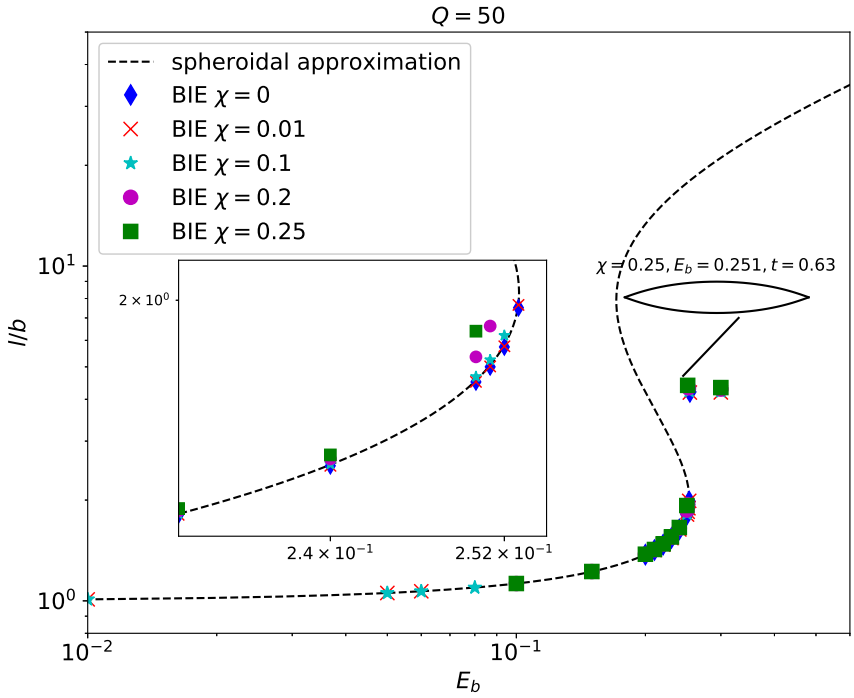

FIG. 6. Steady drop deformation for $Q = 50$ and various χ. Theoretical steady-state response curve using a spheroidal approximation for $\chi = 0$ [14, 37] is shown by a dashed-curve. The subplot provides a zoomed-in view of the numerical data near the first turning point. The drop profile for E_b greater than the turning point on the lower branch exhibits unsteady pointed ends.

to the equilibration time for the Debye layer charge, which is here assumed to be fast, but can evolve more slowly in the model of [14].

It is natural to carry out a slender body analysis when a highly elongated drop is obtained. In Appendix C, we assume a highly deformed drop and obtain an asymptotic approximation of the electric field for a spheroidal drop, see (C15). The field is shown to be almost uniform. Our results serve as a correction to the result in [15] by taking into account the presence of ions. Integration of the field gives the electric potential, and the theoretical drop shape and electrostatic potential are compared to our numerically computed solutions in Figure 7. In the upper panels of the figure, the drop is highly elongated with aspect ratio about 10 (i.e. slenderness parameter $\epsilon = b/l \approx 0.1$). Both the shape and electric potential are in excellent agreement with theory. In the bottom panels, the drop shape is shown to deviate from a spheroid with the same aspect ratio (about 4.4). The interfacial potential is also slightly different from the prediction of slender-body analysis but the agreement is still reasonably good.

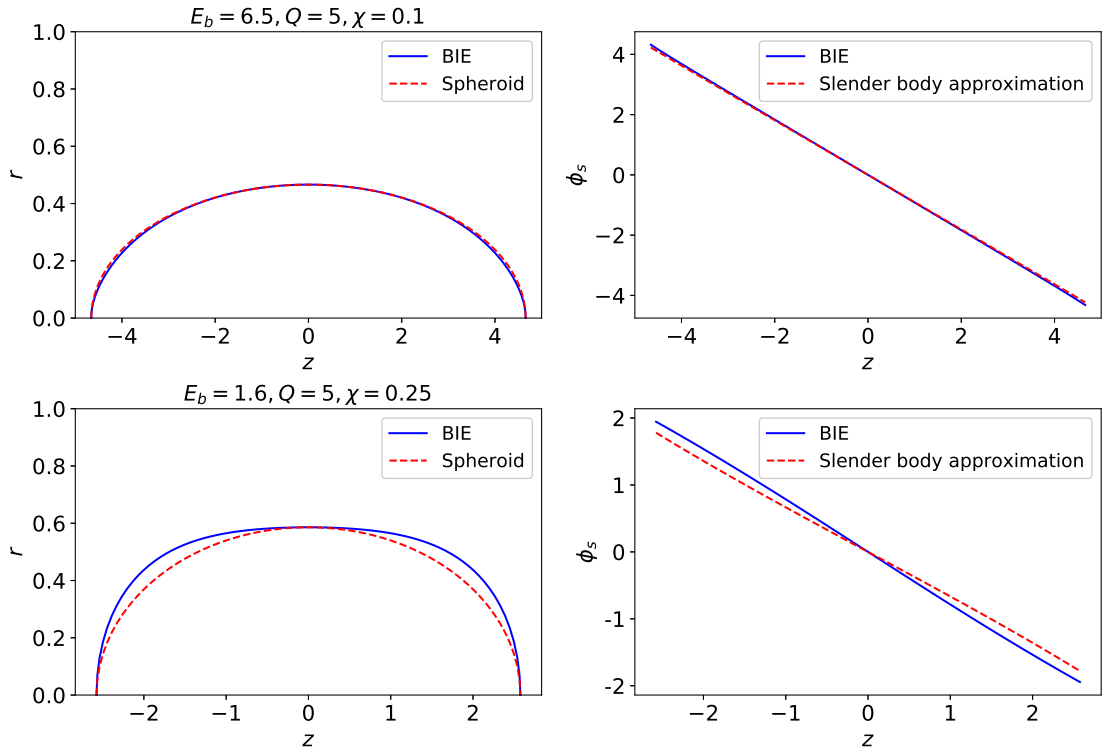

FIG. 7. Comparison of drop shape with a spheroid that has the same aspect ratio. Top left: aspect ratio $l/b \approx 10$ for a slightly conducting drop with $\chi = 0.1$, $E_b = 6.5$, $Q = 5$. Bottom left: aspect ratio $l/b \approx 4.4$ with $\chi = 0.25$, $E_b = 1.6$, $Q = 5$. Right: comparisons between calculated surface potentials and slender body approximation, for same parameter values as in left panels.

B. Breakup behavior

In this section, we investigate drop deformation for parameter values in which steady state solutions do not exist. Several different types of unsteady solution are observed (depending on parameter values), which are classified into three groups: (i) conical end formation, (ii) end-splashing, and (iii) open end stretching: A few case studies are presented before a summary is given.

Conical end formation

In Figure 8, conical end formation is shown for conducting drops with $Q = 50$ and $\chi = 0.1, 1, 10$. In the upper panel of the figure, a time-sequence of unsteady drop shapes are shown for $\chi = 10$, $Q = 50$, starting from an initially spherical shape. In the lower panel, drop

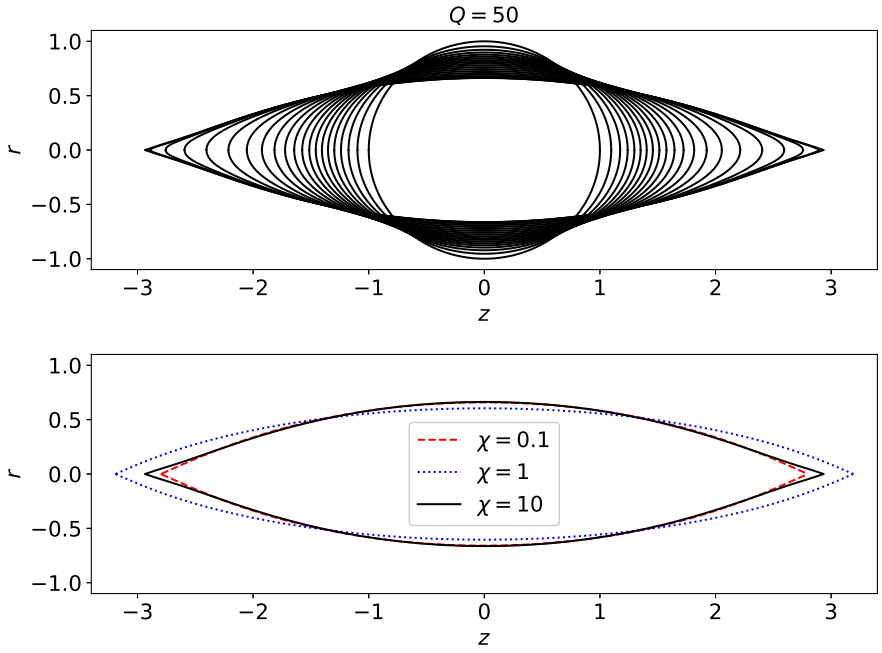

FIG. 8. Upper panel: Evolution of drop with $Q = 50$, $\chi = 10$ and $E_b = 0.26$. Bottom panel: Drop shapes at breakdown of the numerical scheme for $Q = 50$ and $E_b = 0.26$.

shapes at the point at which the simulation is terminated are shown for $\chi = 0.1, 1, 10$, which all show the formation of unsteady conical drop tips that are similar to the shapes reported in [13, 15, 16]. The simulation is terminated when the tip curvature κ_{tip} becomes sufficiently large that the number of grid points and time-step required to resolve the interface make the simulation too computationally costly. It is argued in Appendix C 2, based on equation (C16), that conical end formation can occur only for sufficiently large Q, or more precisely $Q \gtrsim 15$, regardless of χ.

Fontelos et al. [17] present an analysis of conical singularity formation for a charged, perfectly conducting drop in an insulating medium. They find that the singularity formation is self similar with $\kappa_{tip} = O(\tau^{-\delta})$ and $U_{n,tip} = O(\tau^{\delta-1})$, where $\tau = t_s - t$ is the time to singularity formation (i.e., the singularity occurs at $t = t_s$) and δ is a similarity exponent that depends on the opening angle of the cone. Although our model incorporating electrokinetic effects in the drop interior via the linearized Poisson-Boltzmann equation is different from Fontelos et al. [17], this form of the similarity scalings seems to remain unchanged based on our numerical results. We will determine δ from numerical data, but one difficulty in doing so is that the singularity time t_s is unknown. While it can be estimated from

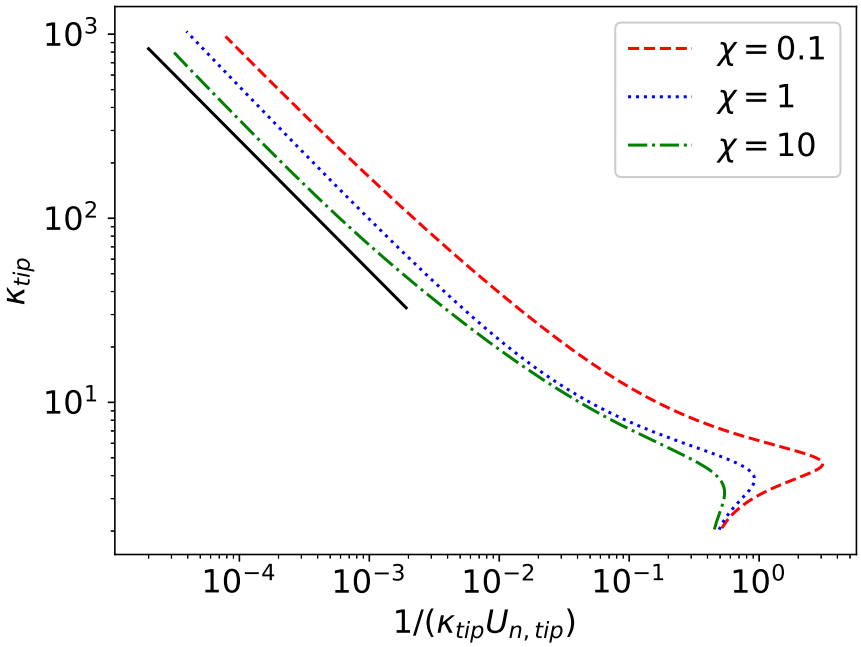

FIG. 9. Evolution of interface tip curvature κ_{tip} versus $1/(\kappa_{tip}U_{n,tip})$ for the three cases in Figure 8. Here, $U_{n,tip}$ is the normal velocity at the tip. Following the scaling law $\kappa_{tip} = O(\tau^{-\delta})$ and $U_{n,tip} = O(\tau^{\delta-1})$ from Fontelos et al. [17], we plot κ_{tip} versus the time to singularity $\tau \sim 1/(\kappa_{tip} \cdot U_{n,tip})$. The estimated or average slope $\delta \approx 0.71$ is shown as a black solid line.

numerical data, we take a different approach. Assuming the above self-similar scalings, then $\tau \sim 1/(\kappa_{tip} \cdot U_{n,tip})$, and since accurate values for κ_{tip} and $U_{n,tip}$ are provided by the numerical data, we can replace τ by $1/(\kappa_{tip} \cdot U_{n,tip})$ in a log-log plot to determine δ. Such a plot of the time evolution of tip curvature κ_{tip} versus $1/(\kappa_{tip} \cdot U_{n,tip})$ for a drop which forms conical tips is shown in Figure 9. The figure shows linear behavior for $\log \kappa_{tip}$ with a slope that is very slightly dependent on χ. We estimate the slope magnitude or similarity exponent to be very near $\delta = 0.71$, which is close to the value of 0.72 reported in Fontelos et al. [17]. Our simulations give slightly different results for the cone angles than Betelú et al. [16] and Fontelos et al. [17]. We find the semi-angles are between $21 \sim 24$ degrees for the different χ values. In the work of Betelú et al. [16], the semi-angle is shown to be dependent on the viscosity ratio and is about 25 degrees for $\lambda = 1$. A slightly different result of about 27.5 degrees is reported in Fontelos et al. [17] (for a different model). While we cannot completely rule out numerical error as a source of the variation of cone angle with χ found here, resolution studies suggest that the computed angles are well resolved. We note

that the current numerical method is only able to resolve about 2 decades of scaling in the space-time neighborhood of the singularity, which is similar to the other cited studies. For much more than this, and for a more detailed investigation of cone angles, it is anticipated that a specialized numerical treatment of the emerging singularity is needed.

End-splashing mode

When χ is large enough (see Figure 13 for precise values), conical end formation is replaced by a small finger that is emitted from the tip, nearly perpendicular to the axis of symmetry or z-axis. This behavior persists even in the highly conducting drop limit of large χ. The interface shape near the ends eventually evolves into a 'snail-head' that forms in the vertical direction. We call this the 'end-splashing mode'. Representative examples of end-splashing are plotted in the top two panels of Figure 10. For these simulations, $N = 320$ and the profile is well resolved up to the point when bulbous ends first form, which marks the onset of snail-head finger formation (see bottom panel). Resolution studies of the fully developed snail head profile, e.g. at the final time in the upper panel of Figure 10, show similar shapes, but slightly decreased snail head length, as resolution is increased. In a 3D view, the drop end looks like a disk or nearly flat cone with a ring rim. This is similar to the so-called dimple formation and lobe-breakup solution reported in Karyappa et al. [53] (see their figure 11 for example). This interface morphology is distinctly different from that observed in Taylor [10], Betelú et al. [16], Grimm and Beauchamp [75] and Fontelos et al. [17], where a Taylor-cone-like solution first develops, then is followed by the ejection of a thin fluid thread in the axial direction.

The end-splashing breakup mode has not been observed in simulations of the leaky dielectric model, although for highly conducting fluids, similar breakup behavior has been reported in experiments and simulations of a perfect conductor model in Karyappa et al. [53]. The experiments have $NaCl$ added to the drop phase, suggesting that ions in the drop may contribute to the fingering instability. More recently, Mohamed et al. [76] observed a similar end-splashing mode in experiments and simulations using an electrokinetic model for conducting fluids in a pendant drop problem, although there it was attributed to the effect of a more viscous fluid in the surrounding medium. In the current study, this behavior is also obtained when the viscosity ratio is one. The middle panel of Figure 10 shows a similar

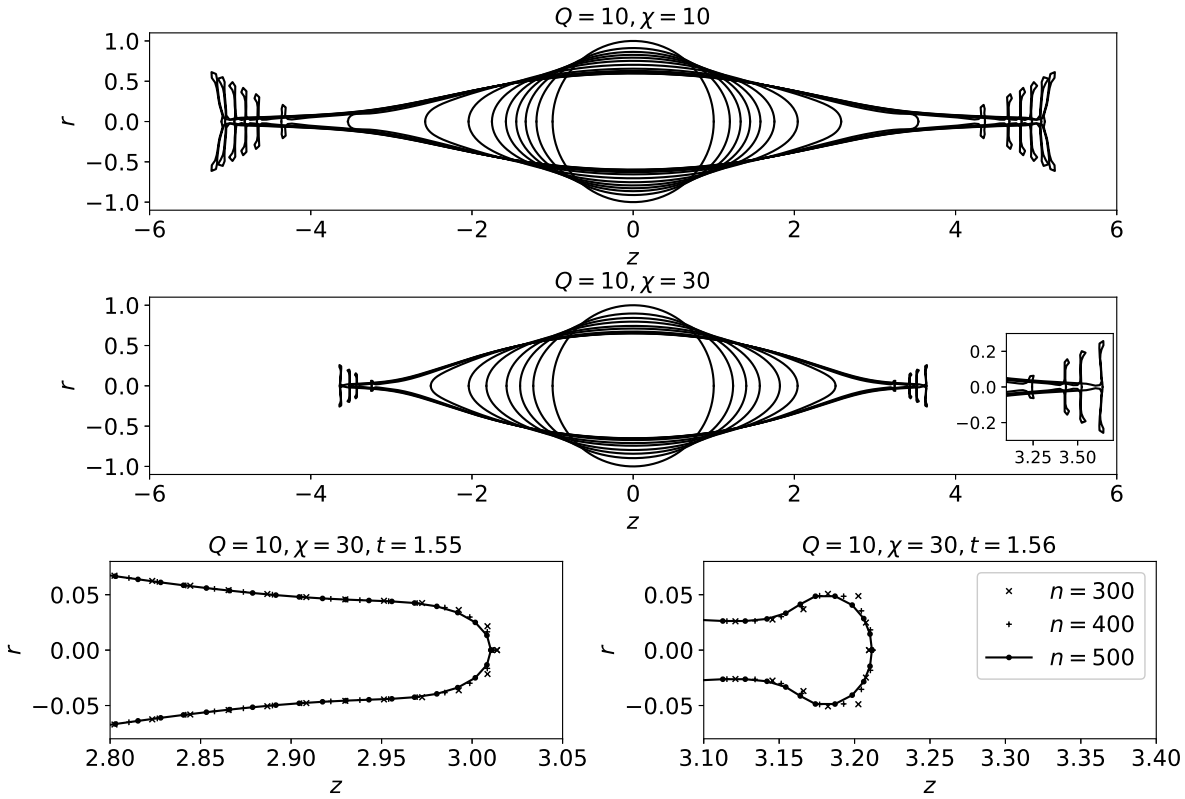

FIG. 10. Breakup of a viscous drop for $Q = 10$ and $E_b = 0.26$ with $\chi = 10$ in upper panel ($t = 0, 0.25, 0.49, 0.74, 0.98, 1.23, 1.47, 1.66, 1.77, 1.83, 1.86, 1.88, 1.90, 1.92, 1.94$) and $\chi = 30$ in the middle panel ($t = 0, 0.30, 0.60, 0.90, 1.20, 1.35, 1.50, 1.56, 1.58, 1.59, 1.61$). The inset of the middle panel show local finger formation before breakup for $\chi = 30$. The lower two panels show tip profiles at different resolution N for $\chi = 30$ at times before (left) and after the snail head is formed (right). The profiles are well-resolved, at least up to the onset of snail formation.

fingering instability for the larger value $\chi = 30$, except that a narrower finger is formed. Our numerical results show a trend of decreasing finger width with increasing χ.

Open end stretching

When both χ and Q are both moderate in size (roughly of the order 10^0 to 10^1) our model exhibits relatively long drops, i.e., with $\epsilon = b/l < 0.01$. One such example is presented in Figure 11 for E_b slightly larger than the critical value for nonexistence of steady sates. The top two panels show the drop shape and interface potential, respectively, while the bottom panel plots the maximum normal velocity. As it evolves, the drop forms a cylindrical central

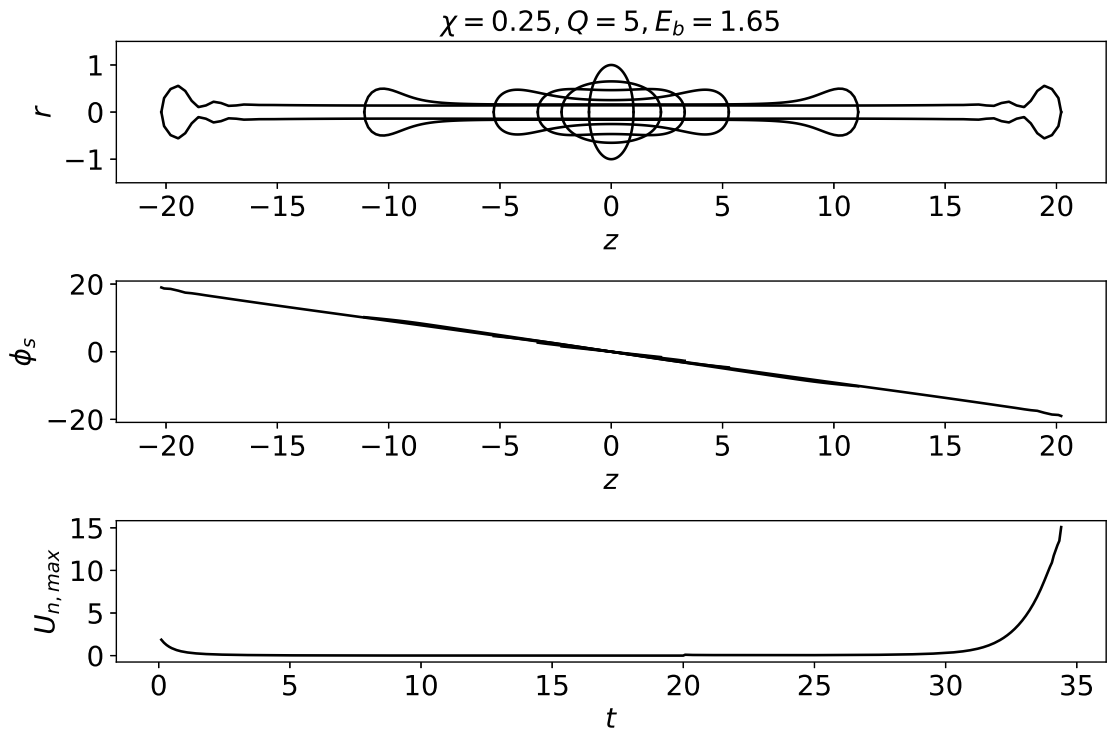

FIG. 11. Breakup of a viscous drop for $Q = 5$ and $E_b = 1.65$ with $\chi = 0.25$. Top: Drop profiles at times $t = 0, 1.73, 29.31, 32.14, 33.56, 34.41$. Middle: interfacial potential ϕ_s versus s, at the same t as top. Bottom: maximum normal velocity versus t.

thread and the electrostatic field is nearly uniform and directed along the axis of symmetry. During the evolution, the normal velocity decreases and the drop nearly settles into an elongated steady state. However, the elongational velocity is reestablished after about $t \approx 30$ as the electric traction overwhelms surface tension. Two 'blobs' develop at the drop ends in a manner similar to the initial stages of the end-splashing mode in Figure 10. However, due to its highly elongated cylindrical thread, we classify this to be a third breakup mode, 'open end stretching'. The simulation in Figure 11 was stopped when the drop aspect ratio exceeded 100. The open-end stretching found here is similar to 'end-pinching' solutions computed using the leaky dielectric model (see, e.g., [30, 33]). We do not find multi-lobe end-pinching solutions, i.e., with internal circulation, like that in Figures 7 and 9 of [30] (see also [33]). We believe these differences may be due to the absence of surface charge and tangential interfacial electric stress in our model.

Summary of breakup modes

We summarize our results in Figures 12 and 13. Figure 12 shows numerically determined curves in $E_b - \chi$ space that separate regions where steady drop shapes exist (or S-regions) from those with purely unsteady dynamics (U-regions). Toward the conducting drop limit, i.e., for sufficiently large Q, the U-region is roughly independent of χ and occurs above $E_b \approx 0.22$. For moderate or small Q, a narrow S-region occurs when χ is sufficiently small, i.e., as the perfect dielectric limit is approached. Alternatively, Figure 13 plots the phase diagram in $Q - \chi$ space with a fixed electric field strength $E_b = 0.5$. The behavior in the U-region is further classified by breakup mode. When $Q \lesssim 15$, we find the S-region for small χ and end-splashing breakup modes (Figure 13(a)) for large χ, while for χ in between we find open end stretching modes as shown at example point Figure 13(c). When $Q \gtrsim 15$, conical end solutions are found for sufficiently small χ (Figure 13(b)), consistent with the asymptotic theory in Appendix C 2, whereas for larger χ we find end-splashing breakup modes.

We conclude this section by noting that only the three aforementioned breakup modes are observed in the current study when the viscosity ratio is unity. Other than end-splashing, solutions which develop topological singularities, i.e., where the drop fractures into two

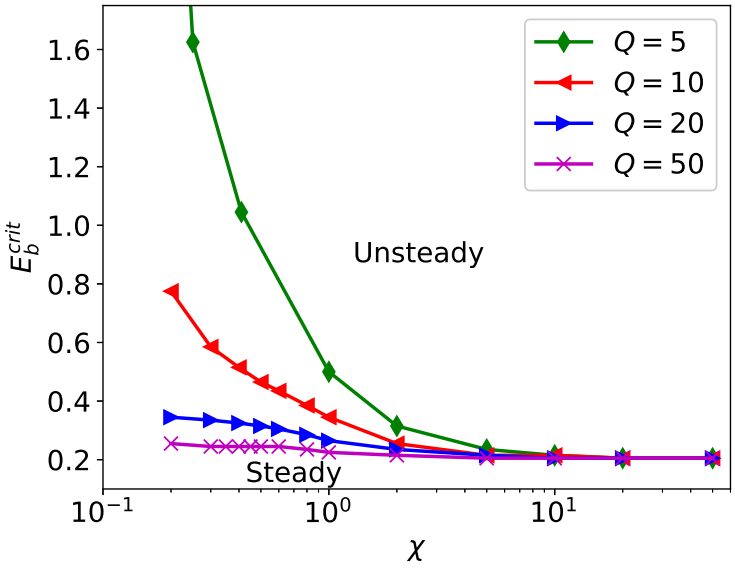

FIG. 12. Boundaries separating steady (S-region) and unsteady (U-region) solutions in the $E_b - \chi$ plane for various Q.

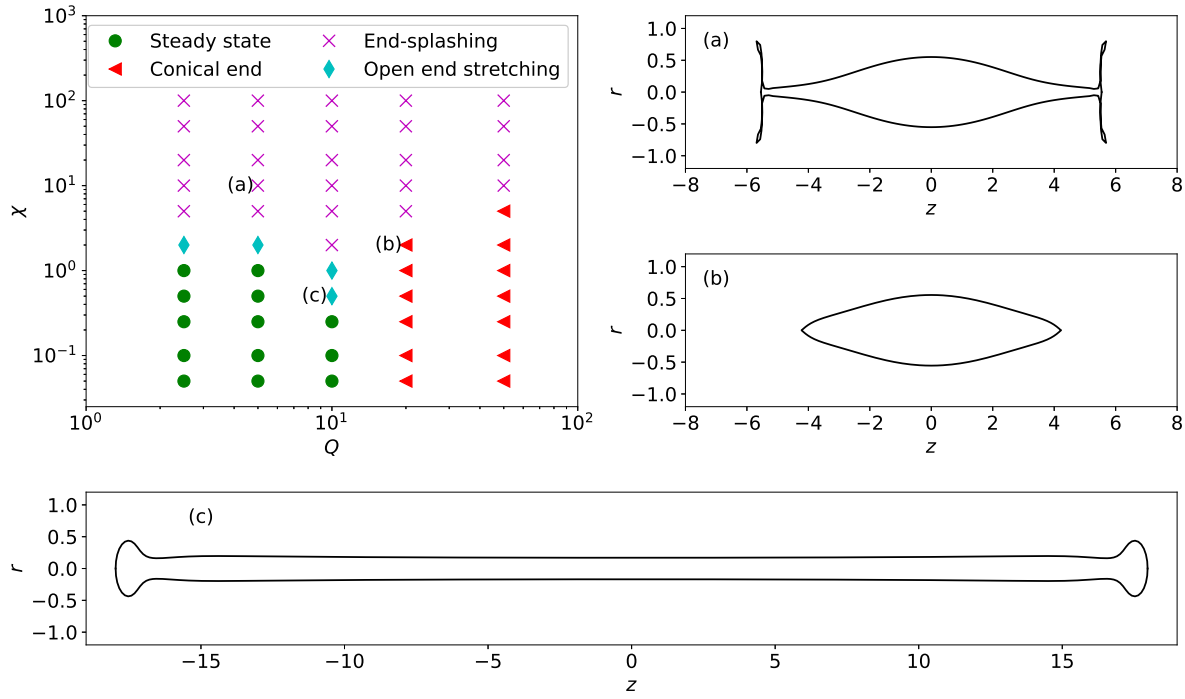

FIG. 13. Phase diagram of steady shapes and breakup modes in $Q-\chi$ space with $E_b = 0.5$. Interface shapes at markers (a)-(c) on the phase diagram are shown in panels at right and below. (a) End-splashing ($Q = 5, \chi = 10$), (b) conical end formation ($Q = 20, \chi = 2$) and (c) open end stretching ($Q = 10, \chi = 0.5$)

or more droplets, are not seen in the electrokinetic model considered here. Preliminary computations show that other breakup modes can occur in our model for $\lambda < 1$, and will be reported elsewhere.

V. CONCLUSION

We have developed a robust and accurate numerical method to evaluate Green's functions for the linearized Poisson-Boltzmann equation and applied it to solve the moving boundary problem for Stokes flow, including electrostatic forces. The method is used to investigate the steady deformation of an electrolyte drop suspended in an insulating fluid medium, for viscosity ratio $\lambda = 1$. We demonstrate that the conducting drop limit can be approached through either $Q \to \infty$ or $\chi \to \infty$, and in these limits, the electric field inside the drop vanishes. For large but finite Q, however, the electric field inside the drop is nonzero and can contribute to the deformation. The perfect dielectric drop limit is $\chi \to 0$, and for

small χ we find that a highly elongated steady drop is possible. For given imposed field strength E_b, the presence of electrolyte enhances the deformation, and increasing χ leading to more deformed drops. When the drop is long and slender, results from our full numerical simulations agree well with approximate solutions based on slender body theory. Finally, we study drop breakup behavior by choosing parameters in the regime where steady solutions no longer exist. In addition to conical end formation, we find other two breakup modes, which we call 'end-splashing' and 'open end stretching'. The type of break up depends on parameter values and an example phase diagram is presented which illustrates the dependence on two of those parameters (Q and χ), for fixed E_b.

Finally, we note that the electrokinetic model and numerical method developed here can provide a framework for extensions that incorporate additional physics, including surface charge or electrolytic effects in the exterior fluid.

ACKNOWLEDGMENTS

MS acknowledges the financial support from National Science Foundation through the grant DMS-1412789, MM acknowledges the financial support from Natural Science Foundation of China (No. 11701428) and "Chen Guang" project supported by Shanghai Municipal Education Commission and Shanghai Education Development Foundation.

Appendix A: Computation of axisymmetric Green's functions and their derivatives

In this section, we present the derivatives of the axisymmetric Green's functions (24) and (22). Gradients of the axisymmetric Green's function for Laplace's equation are given by

$$\frac{\partial G^0}{\partial z} = -\frac{(z-z_0)k^3E(k)}{8\pi(rr_0)^{3/2}(1-k^2)}, \tag{A1}$$

$$\frac{\partial G^0}{\partial r} = -\frac{k^3}{8\pi(rr_0)^{3/2}}\left[\left(\frac{r-r_0}{1-k^2}-\frac{2r_0}{k^2}\right)E(k)+\frac{2r_0}{k^2}K(k)\right], \tag{A2}$$

where $K(k)$ is the complete elliptic integral of the first kind (see (23)) and

$$E(k) = \int_0^{\pi/2}\sqrt{1-k^2\cos^2\theta}\,d\theta \tag{A3}$$

is the complete elliptic integral of the second kind. For the axisymmetric Green's function G^χ of the modified Helmholtz equation, we find that the Green's function gradient is given

by

$$\frac{\partial G^{\chi}}{\partial z} = \frac{k_z}{2\pi(rr_0)^{1/2}} \int_0^{\pi/2} \frac{1+\Lambda\left(1-k^2\cos^2\theta\right)^{1/2}}{\left(1-k^2\cos^2\theta\right)^{3/2}} \exp\left(-\Lambda\left[1-k^2\cos^2\theta\right]^{1/2}\right) d\theta, \tag{A4}$$

$$\frac{\partial G^{\chi}}{\partial r} = \frac{1}{2\pi(rr_0)^{1/2}} \int_0^{\pi/2} \frac{1+\Lambda\left(1-k^2\cos^2\theta\right)^{1/2}}{\left(1-k^2\cos^2\theta\right)^{1/2}} \left(\frac{k_r}{1-k^2\cos^2\theta} - \frac{k}{2r}\right) \times \exp\left(-\Lambda\left[1-k^2\cos^2\theta\right]^{1/2}\right) d\theta. \tag{A5}$$

For the general calculations of Green's functions for Laplace equation, details can be found in Pozrikidis [66].

TABLE I. $\chi = 0.1$, Gauss-Trapezoidal parameters $j = 7$, $k = 6$, $n = j + k + m$

n	Gauss-Trapezoidal			Gauss-Chebyshev		
	G^{χ}	G_z^{χ}	G_r^{χ}	G^{χ}	G_z^{χ}	G_r^{χ}
16	1.95602152	207.50604021	-208.60234657	1.95602514	207.50604303	-208.60234683
32	1.95602152	207.50604021	-208.60234657	1.95602243	207.50604261	-208.60234833
64	1.95602152	207.50604021	-208.60234657	1.95602175	207.50604218	-208.60234839
128	1.95602152	207.50604021	-208.60234657	1.95602158	207.50604176	-208.60234809
256	1.95602152	207.50604021	-208.60234657	1.95602154	207.50604134	-208.60234770
512	1.95602152	207.50604021	-208.60234657	1.95602153	207.50604093	-208.60234730
1024	1.95602152	207.50604021	-208.60234657	1.95602153	207.50604057	-208.60234693

TABLE II. $\chi = 1$

n	Gauss-Trapezoidal			Gauss-Chebyshev		
	G^{χ}	G_z^{χ}	G_r^{χ}	G^{χ}	G_z^{χ}	G_r^{χ}
16	1.66552053	207.50556904	-208.52289051	1.66588210	207.50585107	-208.52291721
32	1.66552054	207.50556904	-208.52289050	1.66561085	207.50580881	-208.52306613
64	1.66552056	207.50556904	-208.52289048	1.66554306	207.50576654	-208.52307180
128	1.66552057	207.50556904	-208.52289048	1.66552612	207.50572433	-208.52304161
256	1.66552057	207.50556904	-208.52289048	1.66552191	207.50568240	-208.52300272
512	1.66552057	207.50556904	-208.52289048	1.66552087	207.50564156	-208.52296267
1024	1.66552057	207.50556904	-208.52289048	1.66552063	207.50560466	-208.52292600

TABLE III. $\chi = 10$

n	Gauss-Trapezoidal			Gauss-Chebyshev		
	G^χ	G_z^χ	G_r^χ	G^χ	G_z^χ	G_r^χ
16	1.12249190	207.47248568	-208.10737309	1.15507371	207.50023604	-208.11656235
32	1.12249346	207.47248566	-208.10737197	1.13128003	207.49634418	-208.12532268
64	1.12249500	207.47248564	-208.10737086	1.12472887	207.49220608	-208.12550479
128	1.12249602	207.47248562	-208.10737012	1.12305031	207.48800774	-208.12247820
256	1.12249628	207.47248562	-208.10736994	1.12262964	207.48382016	-208.11859296
512	1.12249621	207.47248562	-208.10736999	1.12252599	207.47973719	-208.11458941
1024	1.12249620	207.47248562	-208.10737000	1.12250164	207.47604760	-208.11092268

In table I to III, we show data from a computation of G^χ comparing the Gauss-Chebyshev method and Gauss-Trapezoidal method (or Alpert quadrature), for $\chi = 0.1, 1, 10$, and different n or number of quadrature points. The points of evaluation are $(z_0, r_0) = (\cos(\pi/4), \sin(\pi/4))$, $(z, r) = (\cos(\pi/4 + \pi/4096), \sin(\pi/4 + \pi/4096))$, so that (z, r) is slightly different from (z_0, r_0). When $(1 - t^2)^{-1/2}$ is treated as a weight function in (25), the integration, for a regular function $f(x)$, can be done by Gauss-Chebyshev quadrature

$$\int_{-1}^{1} \frac{f(t)}{(1-t^2)^{1/2}} dt = \frac{\pi}{n} \Sigma_{j=1}^{n} f(t_{j,n}) + \frac{2\pi}{2^{2n}(2n)!} f^{(2n)}(\eta), \tag{A6}$$

for some $-1 < \eta < 1$ and

$$t_{j,n} = \cos\left(\frac{2j-1}{2n}\pi\right). \tag{A7}$$

For $\chi = 0.1$, both quadrature methods work well, however, Gauss-Trapezoidal quadrature is more accurate than Gauss-Chebyshev for moderate and large χ, as seen in Table II and III. In particular, when $\chi = 10$, it is seen that convergence is poor for the Gauss-Chebyshev method. For example, G_r^χ obtains only one digit of precision at the largest n. In this paper, we therefore employ Gauss-trapezoidal quadrature since it has performed well in our tests. We have not performed an extensive investigation of quadrature methods, as this is beyond the scope of current paper.

Appendix B: Small deformation theory

Small deformation analysis of an electrolyte droplet immersed in a dielectric fluid and deformed by a nonuniform electric field is provided by [49], from which the following solution for a uniform field can be easily recovered. When the drop is spherical, the general solution for the electric potential is given in spherical radial and polar coordinates $\bar{r}, \bar{\theta}$ by

$$\phi_1 = -A_1(\bar{r})\cos(\bar{\theta}), \quad \phi_2 = -\left(1 - \frac{A_2}{\bar{r}^3}\right)\bar{r}\cos(\bar{\theta}) \tag{B1}$$

with

$$i_1(x) = \frac{x\cosh(x) - \sinh(x)}{x^2}, \tag{B2}$$

$$i_2(x) = \frac{(x^2+3)\sinh(x) - 3x\cosh(x)}{x^3}, \tag{B3}$$

$$A_1(\bar{r}) = \frac{3i_1(\chi\bar{r})}{(Q+2)i_1(\chi) + Q\chi i_2(\chi)}, \tag{B4}$$

$$A_2 = \frac{(Q-1)i_1(\chi) + Q\chi i_2(\chi)}{(Q+2)i_1(\chi) + Q\chi i_2(\chi)}. \tag{B5}$$

When deformability is included, first order perturbation can be used to approximate the shape of the drop. Assuming the shape is perturbed slightly when $E_b \ll 1$, [49] derived an expression for the deformation

$$D_f \approx \frac{3E_b h(\chi, Q)}{4 + E_b h(\chi, Q)} \approx \frac{3}{4}E_b h(\chi, Q) + O(E_b^2) \tag{B6}$$

where

$$h(\chi, Q) = \frac{1}{12Q}\left[(Q-1)(1+2A_2)^2 + (\chi^2 + 1 - Q)A_1^2(r=1)Q\right]. \tag{B7}$$

It is instructive to note some limits in these formulas. First consider the limit of a conducting drop: as $Q \to \infty$ or $\chi \to \infty$, we have $\phi_1(\bar{r}) = 0$ and $\phi_2(\bar{r}) = (r^{-2} - r)\cos\theta$. Inside the drop, both $\phi_{1\bar{r}}$ and $\phi_{1\bar{\theta}}$ tend to zero, that is, the electric field is zero for $\bar{r} < 1$, but on the drop surface there is a nonzero normal component given by $Q\phi_{1\bar{r}} \mid_{\bar{r}=1} = \phi_{2\bar{r}} \mid_{\bar{r}=1} = -3\cos\bar{\theta}$. The surface deformation function satisfies $\lim_{\chi\to\infty} h(\chi, Q) = (12Q)^{-1}(9(Q-1) + 9Q^{-1})$, and $\lim_{Q\to\infty} h(\chi, Q) = 3/4$. In the limit $\chi \to 0$ of a dielectric drop, $\phi_1(\bar{r}) = -(3r/(Q+2))\cos\theta$ and $\phi_2(\bar{r}) = [(Q-1)/(Q+2)](1/r^2 - r)\cos\theta$, from which the electric field is easily obtained by differentiation. The surface deformation function satisfies $\lim_{\chi\to 0} h(\chi, Q) = (3/4)[(Q-1)/(Q+2)]^2$.

Appendix C: Slender body analysis

We carry out slender-body analysis on the boundary-integral equations, following Stone et al. [15],. Define a slenderness parameter $\epsilon = b/l$, where l and b are the half length and half width of drop, respectively. The existing dimensionless equations are adapted for the slender-body scales by making the substitution

$$S \to \frac{\epsilon}{\nu}\hat{S}, \quad z \to \frac{1}{\nu}\hat{z}, \tag{C1}$$

where $\nu = R/l$ and variables with a hat are $O(1)$.

For a slender drop, i.e., $\epsilon = b/l \ll 1$, the electric field inside the drop is to leading order in the axial direction, i.e., $E_t \approx E(z) = \nu\hat{E}(\hat{z})$. As a result, the normal stress balance (11) simplifies to

$$\begin{aligned}\frac{E_b(Q-1)}{2}(QE_{1n}^2 + E_t^2) + \triangle p &= \frac{E_b(Q-1)\nu^2}{2\epsilon^2}(Q\hat{E}_{1n}^2 + \epsilon^2\hat{E}^2) + \triangle\hat{p} \\ &\approx \frac{\nu}{\epsilon\hat{S}} - \epsilon\nu\hat{S}_{\hat{z}\hat{z}} - \frac{\alpha}{2}\phi_1^2,\end{aligned} \tag{C2}$$

where $\hat{r} = \hat{S}(z)$ is the drop surface shape and $\triangle\hat{p}$ is the constant pressure difference between drop interior and exterior. The second term on the right hand side of (C2) is the contribution to surface tension from the axial curvature, which is commonly retained despite being higher order. Since $\nabla \cdot E = -\chi^2\phi_1$, the internal field can be estimated to leading order as

$$\hat{E}_{\hat{r}} \approx -\frac{1}{2}\epsilon^2\hat{S}\left(\hat{E}_{\hat{z}} + \nu^{-2}\chi^2\phi_1\right), \tag{C3}$$

hence (see also [15]),

$$\hat{E}_{1n} \approx -\frac{\epsilon^2}{2\hat{S}}\left(\left(\hat{S}^2\hat{E}\right)_{\hat{z}} + \nu^{-2}\chi^2\hat{S}^2\phi_s\right). \tag{C4}$$

The potential exterior to the slender drop is approximated following [74]. Starting from the boundary integral representation of the exterior potential, we subtract (14) from (13) to obtain

$$\phi_1(\boldsymbol{x}_0) - \phi_\infty + \int_S \phi_1\left(\frac{\partial G_{3D}^\chi}{\partial n} - \frac{\partial G_{3D}^0}{\partial n}\right)dS = \int_S \frac{\partial\phi_1}{\partial n}\left(G_{3D}^\chi - QG_{3D}^0\right)dS, \tag{C5}$$

which is equivalent to the integral-equation used in [15, 33] when $\chi = 0$. Following [77], we focus on the contribution of the integral from $\epsilon\hat{S} \ll |\hat{z} - \hat{z}_0| \ll 1$. For a point on the drop

centerline $(0, z_0)$, the Green's function (24) is expanded before evaluating along drop surface $\hat{r} = \hat{S}$,

$$G_{3D}^{\chi} = \nu \frac{e^{\left(-\frac{\chi}{\nu}\left[(\hat{z}-\hat{z}_0)^2+\epsilon^2\hat{r}^2\right]^{1/2}\right)}}{2\left((\hat{z}-\hat{z}_0)^2+\epsilon^2\hat{r}^2\right)^{1/2}} = \frac{\nu - \chi\left[(\hat{z}-\hat{z}_0)^2+\epsilon^2\hat{r}^2\right]^{1/2} + \frac{\chi^2}{2\nu}\left[(\hat{z}-\hat{z}_0)^2+\epsilon^2\hat{r}^2\right]}{2\left((\hat{z}-\hat{z}_0)^2+\epsilon^2\hat{r}^2\right)^{1/2}} + \cdots \tag{C6}$$

Substituting into (C5) yields

$$\begin{aligned}\phi_1(\hat{z}_0) - \phi_\infty + \frac{\chi^2}{4\nu^2}\int_{-1}^{1}\phi_1 \frac{\epsilon^2\hat{S}^2}{\left((\hat{z}-\hat{z}_0)^2+\epsilon^2\hat{S}^2\right)^{1/2}}d\hat{z} \\ = -(1-Q)\int_{-1}^{1}\frac{\hat{S}\hat{E}_{1n}}{2\left((\hat{z}-\hat{z}_0)^2+\epsilon^2\hat{S}^2\right)^{1/2}}d\hat{z} - \frac{\chi}{2\nu}\int_{-1}^{1}\hat{E}_{1n}\hat{S}d\hat{z} + \cdots\end{aligned} \tag{C7}$$

which is further evaluated to be

$$\begin{aligned}\phi_1 - \phi_\infty + \frac{\epsilon^2\chi^2\ln(1/\epsilon)}{2\nu^2}\phi_1\hat{S}^2 \\ =(1-Q)\frac{\epsilon^2\ln(1/\epsilon)}{2}\left((\hat{S}^2\hat{E})_{\hat{z}} + \nu^{-2}\chi^2\hat{S}^2\phi_1\right) - \frac{\chi}{2\nu}\int_{-1}^{1}\hat{E}_{1n}\hat{S}d\hat{z} + \cdots .\end{aligned} \tag{C8}$$

This is coupled with the equation for drop volume,

$$\int_{-1}^{1}\hat{S}^2 d\hat{z} = \frac{4\nu^3}{3\epsilon^2}, \tag{C9}$$

which readily yields $\nu = \epsilon^{2/3}$.

1. Electric field inside a spheroid

For a spheroid, $\hat{S}^2 + \hat{z}^2 = 1$ and equation (C8) with $\chi = 0$ is satisfied by a uniform electric field E_{1D},

$$E_{1D} = \frac{1}{1+\epsilon^2\ln(1/\epsilon)\,(Q-1)} \sim 1 - \epsilon^2\ln(1/\epsilon)\,(Q-1) + \cdots \tag{C10}$$

which agrees with the approximation in Stone et al. [15]. For order one $\chi > 0$ and $\chi/\nu \gg 1$, (C8) at leading order (after taking one derivative with respect to $\hat{z}$) becomes

$$-\hat{E}_{1D} + \frac{1}{\nu} \approx -Q\frac{\epsilon^2\chi^2\ln(1/\epsilon)}{2\nu^2}\left(\phi_1\hat{S}^2\right)_{\hat{z}}. \tag{C11}$$

Assume $\hat{E}_{1D} \sim \nu^{-1} + \Psi(\hat{z})$ so that $\phi_1 \sim -\nu^{-1}\hat{z} - \int^{\hat{z}} \Psi(s)ds$. After denoting $F = \int^{\hat{z}} \Psi(s)ds$ we arrive at

$$-F = Q\frac{\epsilon^2\chi^2\ln(1/\epsilon)}{2\nu^2}\left[(1-\hat{z}^2)\left(\nu^{-1}\hat{z}+F\right)\right]. \tag{C12}$$

This is rewritten as

$$F = -K\frac{\hat{z}}{\nu}\frac{1-\hat{z}^2}{1+K(1-\hat{z}^2)} \sim -K\frac{\hat{z}}{\nu}(1-\hat{z}^2) \tag{C13}$$

where $K = Q\frac{\chi^2\epsilon^2\ln(1/\epsilon)}{2\nu^2} \ll 1$. After some algebra, we arrive at an approximation for the electric field inside the drop, which holds for $Q \ll \frac{\nu^2}{\chi^2\epsilon^2\ln(1/\epsilon)}$

$$\begin{aligned}\hat{E}_{1D} &= \nu^{-1} + F_{\hat{z}} - \epsilon^2\ln(1/\epsilon)\,(Q-1)\,\nu^{-1} + \cdots \\ &= \frac{1}{\nu} - Q\frac{\epsilon^2\chi^2\ln(1/\epsilon)}{2\nu^3}(1-3\hat{z}^2) - \frac{\epsilon^2\ln(1/\epsilon)\,(Q-1)}{\nu} + \cdots\end{aligned} \tag{C14}$$

After using $E = \nu\hat{E}$, the electric field is recovered under the original scaling to yield

$$E_{1D} \approx 1 - \epsilon^2\ln(1/\epsilon)\,(Q-1) - Q\frac{\epsilon^{4/3}\chi^2\ln(1/\epsilon)}{2}(1-3(\epsilon^{2/3}z)^2). \tag{C15}$$

This is consistent with Stone et al. [15] for $\chi = 0$, and the term with χ provides a correction due to the presence of ions. The field is used to compare to the full boundary-integral simulation when the drop is elongated.

2. Drop with conical ends

For a drop with conical end, locally $\hat{S} \sim 1 - \hat{z}$ and $\epsilon = \tan\theta_0$. It is seen in normal stress balance (C2) that $E \sim (1-\hat{z})^{-1/2}$, then (C8) shows the terms with χ serve as higher order corrections, and we still have the same equation from Stone et al. [15]

$$Q = 1 - \frac{8}{3\tan^2\theta_0\ln(\tan\theta_0)}, \tag{C16}$$

which reflects a local balance of force contributions from the electric field and surface curvature. Therefore, to leading order, the formation of a conical drop is independent of χ, i.e. the influence of ions. Thus, as for a drop without electrolyte, a conical end is only expected when Q is sufficiently large regardless of χ. To be specific, Stone et al. [15] gives a minimum Q around 15.5, above which conical tip is possible.

Finally, we note that the slender drop shape can be analyzed by coupling (C8), (C2) and (C9) (see Stone et al. [15], Sherwood [78], Rhodes and Yariv [79]). Our preliminary results show a mild singularity between a conical and a rounded end exists (same in [78, 79]) and $E_b(Q-1)\epsilon^{7/3}\ln(1/\epsilon) \sim O(1)$. However, we do not pursue this further in current study as the predicted shape using slender-body is usually in poor comparison with the full simulation.

---

[1] J. R. Melcher. *Continuum Electromechanics*. MIT Press, 1981.

[2] J. R. Melcher and G. I. Taylor. Electrohydrodynamics: a review of the role of interfacial shear stresses. *Ann. Rev. Fluid Mech.*, 1:111–146, 1969.

[3] C.-Y. Lee, C.-L. Chang, Y.-N. Wang, and L.-M. Fu. Microfluidic mixing: a review. *Int. J. Mol. Sci.*, 12:3263–3287, 2011.

[4] A. M. Ganán-Calvo, J. M. López-Herrera, M. A. Herrada, A. Ramos, and J. M. Montanero. Review on the physics electrospray: from electrokinetics to the operating conditions of single and coaxial Taylor cone-jets, and AC electrospray. *J. Aerosol Sci.*, 125:32–56, 2018.

[5] P. M. Vlahovska. Electrohydrodynamics of drops and vesicles. *Ann. Rev. Fluid Mech.*, 51: 305–330, 2019.

[6] J. Zeleny. Instability of electrified liquid surfaces. *Phys. Rev.*, 10:1, 1917.

[7] W. A. Macky. Some investigations on the deformation and breaking of water drops in strong electric fields. *Proc. R. Soc. Lond. A*, 133:565–587, 1931.

[8] C. T. R. Wilson and G. T. Taylor. The bursting of soap-bubbles in a uniform electric field. *Math. Proc. Cambridge Philos. Soc.*, 22:728–730, 1925.

[9] R. S. Allan and S. G. Mason. Particle behavior in shear and electric fields I. deformation and burst of fluid drops. *Proc. R. Soc. Lond. A*, 267:45–61, 1962.

[10] G. I. Taylor. Disintegration of water drops in an electric field. *Proc. R. Soc. Lond. A*, 280: 383–397, 1964.

[11] S. Torza, R. G. Cox, and S. G. Mason. Electrohydrodynamic deformation and burst of liquid drops. *Phil. Trans. R. Soc. Lond. A*, 269:295–319, 1971.

[12] C. G. Garton and Z. Krasucki. Bubble in insulating liquids: stability in an electric field. *Proc. R. Soc. Lond. A*, 280:211–226, 1964.

[13] J. D. Sherwood. Breakup of fluid droplets in electric and magnetic fields. *J. Fluid Mech.*,

188:133–146, 1988.

[14] R. Pillai, J. D. Berry, D. J. E. Harvie, and M. R. Davidson. Electrolytic drops in an electric field: a numerical study of drop deformation and breakup. *Phys. Rev. E*, 92:013007, 2015.

[15] H. A. Stone, J. R. Lister, and M. P. Brenner. Drops with conical ends in electric and magnetic fields. *Proc. R. Soc. Lond. A*, 455:329–347, 1999.

[16] S. I. Betelú, M. A. Fontelos, U. Kindelan, and O. Vantzos. Singularities on charged viscous droplets. *Phys. Fluids*, 18:051706, 2004.

[17] M. A. Fontelos, U. Kindelan, and O. Vantzos. Evolution of neutral and charged droplets in an electric field. *Phys. Fluids*, 20:092110, 2008.

[18] N. Gawande, Y. S. Mayya, and R. M. Thaokar. Numerical study of Rayleigh fission of a charged viscous liquid drop. *Phys. Rev. Fluids*, 2:113603, 2017.

[19] R.T. Collins, J.J. Jones, M.T. Harris, and O.A. Basaran. Electrohydrodynamic tip streaming and emission of charged drops from liquid cones. *Nat. Phys.*, 4:149–154, 2008.

[20] Juan Fernández de la Mora. The fluid dynamics of taylor cones. *Ann. Rev. Fluid Mech.*, 39: 217–243, 2007.

[21] G. I. Taylor. Studies in electrohydrodynamics. the circulation produced by a drop in electric field. *Proc. R. Soc. Lond. A*, 291:159–166, 1966.

[22] R. V. Craster and O. Matar. Electrically induced pattern formation in thin leaky dielectric films. *Phys. Fluids*, 17:032104, 2005.

[23] D. Tseluiko, M. G. Blyth, D. T. Papageorgiou, and J.-M. Vanden-Broeck. Effect of an electric field on film flow down a corrugated wall at zero Reynolds number. *Phys. Fluids*, 20:042103, 2008.

[24] A. J. Mestel. Electrohydrodynamic stability of a highly viscous jet. *J. Fluid Mech.*, 312: 311–326, 1996.

[25] M. M. Hohman, M. Shin, G. Rutledge, and M. P. Brenner. Electrospinning and electrically forced jets. I. stability theory. *Phys. Fluids*, 13:2201, 2001.

[26] Q. Wang. Breakup of a viscous poorly conducting liquid thread subject to a radial electric field at zero Reynolds number. *Phys. Fluids*, 24:102102, 2012.

[27] Z. Ding, T. N. Wong, and H. Li. Stability of two immiscible leaky-dielectric liquids subjected to a radial electric field in an annulus duct. *Phys. Fluids*, 25:124103–20, 2013.

[28] Q. Wang and D. T. Papageorgiou. Using electric fields to induce patterning in leaky dielectric

fluids in a rod-annular geometry. *IMA J. Appl. Math.*, 83:24–52, 2018.

[29] R. T. Collins, K. Sambath, M. T. Harris, and O. A. Basaran. Universal scaling laws for the disintegration of electrified drops. *Proc. Nat. Acad. of Sci.*, 110(13):4905–4910, 2013.

[30] Rajarshi Sengupta, Lynn M Walker, and Aditya S Khair. The role of surface charge convection in the electrohydrodynamics and breakup of prolate drops. *J. Fluid Mech.*, 833:29–53, 2017.

[31] J. Q. Feng and T. C. Scott. A computational analysis of electrohydrodynamics of a leaky dielectric drop in an electric field. *J. Fluid Mech.*, 311:289–326, 1996.

[32] J. Hua, L. K. Lim, and C.-H. Wang. Numerical simulation of deformation/motion of a drop suspended in viscous liquids under influence of steady electric fields. *Phys. Fluids*, 20(11): 113302, 2008.

[33] E. Lac and G. M. Homsy. Axisymmetric deformation and stability viscous drop in a steady electric field. *J. Fluid Mech.*, 590:239–264, 2007.

[34] J.-W. Ha and S.-M. Yang. Deformation and breakup of Newtonian and non-Newtonian conducting drops in an electric field. *J. Fluid Mech.*, 405:131–156, 2000.

[35] J.-W. Ha and S.-M. Yang. Elecrohydrodynamics and electrorotation of a drop with fluid less conductive than that of the ambient fluid. *Phys. Fluids*, 12:764–772, 2000.

[36] O. Vizika and D. A. Saville. The electrohydrodynamic deformation of drops suspended in liquids in stead and oscillatory electric fields. *J. Fluid Mech.*, 239:1–21, 1992.

[37] D. A. Saville. Electrohydrodynamics: the Taylor-Melcher leaky dielectric model. *Ann. Rev. Fluid Mech.*, 29:27–64, 1997.

[38] P. M. Vlahovska. Electrodynamic instabilities o f viscous drops. *Phys. Rev. Fluids*, 1:060504, 2016.

[39] J. C. Baygents and D. A. Saville. The circulation produced in a drop by an electric field: a high field strength electrokinetic model. *Drops & Bubbles, Third International Colloquium, Monterey 1988 (ed. T. Wang), AIP Conference Proceedings*, 7:7 – 17, 1989.

[40] Y. Mori and Y-N. Young. From electrodiffusion theory to the electrohydrodynamics of leaky dielectrics through the weak electrolyte limit. *J. Fluid Mech.*, 855:67–130, 2018.

[41] A. J. Pascall and T. M. Squires. Electrokinetics at liquid/liquid interfaces. *J. Fluid Mech.*, 684:163–191, 2011.

[42] O. Schnitzer and E. Yariv. The Taylor-Melcher leaky dielectric model as a macroscale electrokinetic description. *J. Fluid Mech.*, 773:1–33, 2015.

[43] J. D. Berry, M. R. Davidson, and D.J. E. Harvie. A multiphase electrokinetic flow model for electrolytes with liquid/liquid interfaces. *J. Comp. Phys.*, 251:209–222, 2013.

[44] R. Pillai, J. D. Berry, D. J. E. Harvie, and M. R. Davidson. Electrokinetics of isolated electrified drops. *Soft Matter*, 12:3310–3325, 2016.

[45] J. D. Davidson, M. R .and Berry and D. J. E. Harvie. Numerical simulation of the deformation of charged drops of electrolyte. *Advances in Fluid Mechanics X*, 82:203–214, 2014.

[46] J. M. López-Herrera, A. M. Gañán-Calvo, S. Popinet, and M. A. Herrada. Electrokinetic effects in the breakup of electrified jets: A volume-of-fluid numerical study. *Int. J. of Multiphase Flow*, 71:14–22, 2015.

[47] R. Pillai, J. D. Berry, D. J. E. Harvie, and M. R. Davidson. Electrophoretically mediated partial coalescence of a charged microdrop. *Chem. Eng. Sci.*, 169:273–283, 2017.

[48] T. M. Squires and S. R. Quake. Microfluidics: Fluid physics at the nanoliter scale. *Rev. Mod. Phys.*, 77(3):977, 2005.

[49] C. K. Hua, D. W. Lee, and I. S. Kang. Analyses on a charged electrolyte droplet in a dielectric liquid under non-uniform electric fields. *Colloids and Surfaces A: Physicochem. Eng. Aspects*, 372:86–97, 2010.

[50] M. J. Miksis. Shape of a drop in an electric field. *Phys. Fluids*, 24:1967–1972, 1981.

[51] N. Dubash and A. J. Mestel. Behavior of a conducting drop in a highly viscous fluid subject to an electric field. *J. Fluid Mech.*, 581:469–493, 2007.

[52] S. D. Deshmukh and R. M. Thaokar. Deformation, breakup and motion of a perfect dielectric drop in a quadrupole electric field. *Phys. Fluids*, 24:032105, 2012.

[53] R. B. Karyappa, S. D. Deshmukh, and R. M. Thaokar. Breakup of a conducting drop in a uniform electric field. *J. Fluid Mech.*, 754:550–589, 2014.

[54] D. Das and D. Saintillan. A nonlinear small-deformation theory for transient droplet electrohydrodynamics. *J. Fluid Mech.*, 810:225–253, 2017.

[55] P. M. Young and P. G. Martinsson. A direct solver for the rapid solution of boundary integral equations on axisymmetric surfaces in three dimensions. *Technical report, University of Colorado at Boulder, Department of Applied Mathematics*, page arXiv preprint arXiv:1002.2001, 2010.

[56] A. S. Mohamed, J. M. Lopez-Herrera, M. A. Herrada, L. B. Modesto-Lopez, and A. M. Ganan-Calvo. Effect of a surrounding liquid environment on the electrical disruption of pendant

droplets. *Langmuir*, 32(27):6815–6824, 2016.

[57] M. R. Wright. *An Introduction to Aqueous Electrolyte Solutions*. Wiley, 2007.

[58] E. J. Hinch and J. D. Sherwood. The primary electroviscous effect in a suspension of spheres with thin double layers. *J. Fluid Mech.*, 132:337–347, 1983.

[59] D. T. Conroy, R. V. Craster, O. Matar, and D. T. Papageorgiou. Dynamics and stability of an annular electrolyte film. *J. Fluid Mech.*, 656:481–506, 2010.

[60] M. Mao, J. D. Sherwood, and S. Ghosal. Electro-osmotic flow through a nanopore. *J. Fluid Mech.*, 749:167–183, 2014.

[61] R. W. O'Brien and L. R. White. Electrophoretic mobility of a spherical colloidal particle. *J. Chem. Soc. Faraday Trans. 2*, 74:1607–1626, 1978.

[62] J. C. Baygents and D. A. Saville. Electrophoresis of drops and bubbles. *J. Chem. Soc. Faraday Trans.*, 87:1883–1898, 1991.

[63] J. D. Sherwood and H. A. Stone. Electrophoresis of a thin charged disk. *Phys. Fluids*, 7:697, 1994.

[64] R. Kress. *Linear Integral Equations*. Springer, 2014.

[65] C. Pozrikidis. *Boundary Integral and Singularity Method for Linearized Viscous Flow*. Cambridge Universiy Press, 1992.

[66] C. Pozrikidis. *A Practical Guide to Boundary Element Method with the Software Library BEMLIB*. CHAPMAN & HALL/CRC, 2002.

[67] J. Priede and G. Gerbeth. Boundary-integral method for calculating poloidal axisymmetric ac magnetic fields. *IEEE Trans. Magn.*, 42:301–308, 2006.

[68] B. K. Alpert. Hybrid gauss-trapezoidal quadrature rules. *SIAM Journal on Scientific Computing*, 20(5):1551–1584, 1999.

[69] Q. Wang and D. T. Papageorgiou. Dynamics of a visous thread surrounded by another viscous fluid in a cylindrical tube under the action of a radial electric field: Breakup and touchdown singularities. *J. Fluid Mech.*, 683:27–56, 2011.

[70] H. A. Stone and L. G. Leal. The effects of surfactants on drop deformation and breakup. *J. Fluid Mech.*, 220:161–186, 1990.

[71] M. R. Booty, D. T. Papageorgiou, M. Siegel, and Q. Wang. Long-wave equations and direct simulations for the breakup of a fluid thread surrounded by an immiscible viscous fluid. *IMA J. Appl. Math*, 78:851–867, 2013.

[72] Q. Wang, M. Siegel, and M. R. Booty. Numerical simulation of drop and bubble dynamics with soluble surfactant. *Phys. Fluids*, 26:052102, 2014.

[73] P. F. Salipante and P. M. Vlahovska. Electrodynamics of drops in strong uniform DC electric fields. *Phys. Fluids*, 22:112110, 2010.

[74] A. Acrivos and J. M. Rallison. A numerical study of the deformation and burst of a viscous drop in an extensional flow. *J. Fluid Mech.*, 89:191–200, 1978.

[75] R. L. Grimm and J. L. Beauchamp. Dynamics of field-induced droplet ionization: Time-resolved studies of distortion, jetting, and progeny formation from charged and neutral methanol droplets exposed to strong electric fields. *J. Phys. Chem. B*, 109:8244–8250, 2005.

[76] A. S. Mohamed, J.M. Lopez-Herrera, M.A. Herrada, L.B. Modesto-Lopez, and A. M. Ganan-Calvo. Effect of a surrounding liquid environment on the electrical disruption of pendant droplets. *Langmuir*, 32:6815–6824, 2016.

[77] E. J. Hinch. *Perturbation Methods*. Cambridge Universiy Press, 1991.

[78] J. D. Sherwood. The deformation of a fluid drop in an electric field: a slender-body analysis. *J. Phys. A*, 24:4047–4053, 1991.

[79] D. Rhodes and E. Yariv. The elongated shape of a dielectric drop deformed by a strong electric field. *J. Fluid Mech.*, 664:286–296, 2010.